International Journal of Multiphase Flow 197 (2026) 105629

Contents lists available at ScienceDirect

International Journal of Multiphase Flow

journal homepage: www.elsevier.com/locate/ijmulflow

Study of hydrodynamic forces on a finite particle attached to a wall in a confined Couette flow

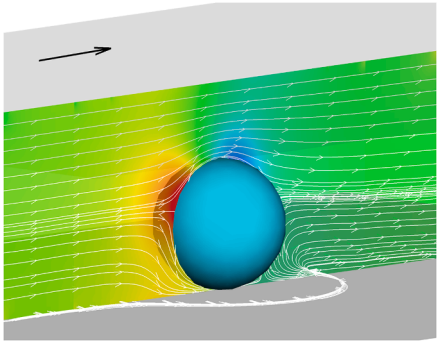
Kun Meng [a], Binbin Shan [a], Yan Cui [a,*], Peng Gao [a], Chengjun Zhang [a], Xuyao Mao [b], Jure Ravnik [c], Matjaž Hriberšek [c], Yinshui Liu [a]

[a] School of Mechanical Science and Engineering, Huazhong University of Science and Technology, Luoyu Road 1037, 430074, Wuhan, China
[b] Wuhan Second Ship Design and Research Institute, 19 Yangqiaohu Ave., 430205, Wuhan, China
[c] Faculty of Mechanical Engineering, University of Maribor, Smetanova 17, SI-2000, Maribor, Slovenia

HIGHLIGHTS

- This study employs GPU-accelerated Lattice Boltzmann simulations to investigate the effects of wall confinement on hydrodynamic forces and the detachment mechanisms of a finite-sized spherical particle attached to a wall in Couette flow. The key findings are highlighted as follows.
- Wall confinement deflects streamlines downward and shifts stagnation points upward, resulting in an increased drag coefficient, a significantly reduced lift coefficient, and a slight increase in the torque coefficient.
- Rolling is identified as the most readily initiated detachment mechanism, and its critical particle Reynolds number decreases as wall confinement intensifies.
- Empirical correlations for the drag, lift, and torque coefficients in confined Couette flow are established by introducing wall-confinement correction factors, and high-accuracy correlations are proposed for particle Reynolds numbers less than or equal to 40 and height-to-size ratios greater than or equal to 1.5.
- It is observed that when the height-to-size ratio exceeds 6, the wall confinement effects on drag and torque become negligible, whereas the suppression of vertical velocity persists, rendering the lift coefficient more sensitive to height-to-size ratio at low particle Reynolds number.

GRAPHICAL ABSTRACT



* Corresponding author.
E-mail address: yan_cui@hust.edu.cn (Y. Cui).

https://doi.org/10.1016/j.ijmultiphaseflow.2026.105629
Received 11 October 2025; Received in revised form 31 December 2025; Accepted 22 January 2026
Available online 23 January 2026
0301-9322/© 2026 Elsevier Ltd. All rights are reserved, including those for text and data mining, AI training, and similar technologies.

ARTICLE INFO

Keywords:
Lattice Boltzmann method
Particle detachment
Confined Couette flow
Hydrodynamic forces
Finite-sized particle

ABSTRACT

Contaminant particles adhering to walls within narrow fluid clearances significantly degrade the performance and service life of precision systems such as hydraulic components and microsensors. This study investigates the effects of wall confinement on hydrodynamics and particle detachment in a Couette flow, where a spherical particle is attached to the bottom wall and subject to the influence of the top wall. Results demonstrate that confinement deflects streamlines downward and shifts stagnation points upward, thereby reducing flow velocity beneath the particle while accelerating it above. The enhanced particle blockage effect increases both the drag and torque coefficients, while the suppression of vertical velocity markedly reduces the lift coefficient. Phase diagrams identify the critical particle Reynolds numbers for three initial detachment modes (rolling, sliding, and lifting), revealing that rolling detachment is the most readily initiated. Empirical correlations for the force and torque coefficients in confined Couette flow are proposed, along with an algorithm for determining the critical particle Reynolds numbers. These tools can be integrated into Eulerian–Lagrangian computational frameworks to improve the efficiency and accuracy of predicting contaminant particle detachment in precision fluid systems.

1. Introduction

Couette flows are commonly observed in micro accelerometers, inertial sensors, resonant filters, and hydraulic components (Ye et al., 2003; Tang et al., 2008; Yin et al., 2017; Blaauw et al., 2025). For example, in piston pumps, the piston moves while the cylinder barrel remains stationary, resulting in Couette flows (Chen et al., 2016). In these scenarios, the gap height of the Couette flow is minimal, allowing finite-sized contaminant particles in the fluid to accumulate on the wall, which can lead to increased friction or wear of the component (Chen et al., 2024; Liu et al., 2025). Therefore, studying finite-sized particle detachment within clearance gaps can be effectively simplified by analysing finite-sized particle detachment from the wall in confined Couette flows, enhancing the reliability and service life of components and microsensors.

The practical motivation is clear, yet a fundamental understanding requires first examining particle-wall interactions in simpler flow configurations (Wang et al., 2023; Goyal et al., 2024). The hydrodynamic forces and torques acting on a spherical particle in contact with a smooth wall within unconfined linear shear flows have been extensively studied, forming a coherent evolutionary path from theoretical foundations to practical applications (Vasseur and Cox, 1976; Magnaudet et al., 2003; Happel and Brenner, 2012; Wang et al., 2025). This research trajectory commenced with Stokes' (1851) pioneering work quantifying drag in Stokes flow, followed by Goldman et al. (1967) and O'Neill's (1968) analytical solution for wall-bounded spheres. The field subsequently progressed to finite Reynolds number regimes through the integration of semi-empirical approaches, notably Schiller and Naumann's (1933) correlation, culminating in comprehensive Direct Numerical Simulation (DNS) based formulations by Zeng et al. (2009) that bridge theoretical precision with practical applicability. Recent extensions by Ekanayake et al. (2020) further refined these correlations for complex scenarios involving particle rotation and wall proximity effects.

Regarding the lift coefficient, Saffman (1965) provided an analytical solution for a sphere in an unbounded linear shear flow, which is valid under conditions of very high shear rates. This theory was later extended to moderate shear rates by McLaughlin (1991) and developed to droplets of arbitrary drop-to-fluid viscosity ratio by Legendre and Magnaudet (1997). In addition, Leighton and Acrivos (1985) found that the lift coefficient for a sphere fixed to a smooth wall in a linear shear flow is a constant value of 5.87 (for the definition of the lift coefficient, see Eq. (2) in Section 2), which subsequently decreases at finite particle Reynolds numbers. Furthermore, Zeng et al. (2009) proposed an empirical correlation for the lift coefficient of a fixed sphere in contact with a wall in a linear shear flow. Particles immersed in a wall-bounded shear flow may slide along the wall and simultaneously rotate, both of which can significantly modify the lift. Such situations were considered by Cherukat and McLaughlin (1994) and Krishnan and Leighton (1995) for a solid particle in the low-Reynolds-number limit. An extension of these analyses to droplets with arbitrary drop-to-fluid viscosity ratios was performed by Magnaudet et al. (2003). However, all these studies assume that the wall lies in the "*inner*" region of the disturbance, where viscous effects dominate. Configurations in which the wall lies in the "*outer*" region of the disturbance were first examined by McLaughlin (1993) and later by Shi et al. (2021). Nevertheless, it was not until the works of Ekanayake et al. (2020, 2021) that empirical correlations for the lift coefficient became available for a freely rotating sphere at nearly arbitrary particle–wall separations in a linear shear flow. Gao et al. (2024) conducted a study on the lift forces acting on small inertial particles within turbulent wall flows, as well as the impact of these lift forces in the vicinity of the wall. Their findings suggest that for inner-scaled diameters (i.e., the ratio of a particle's physical diameter to the viscous length scale) of approximately one or greater, lift forces significantly influence near-wall flow dynamics of particles.

In the context of linear shear flows, the fluid shear rate and the asymmetry of the flow field generate a hydrodynamic torque on the particle. Goldman et al. (1967) were the first to present an analytical solution for the torque coefficient of a sphere in close contact with a wall in Stokes flow. Zeng et al. (2009) found that as the particle Reynolds number increases, the torque coefficient for the spherical particle adhered to the smooth wall experiences a significant reduction. Additionally, as the particle moves further away from the wall, the torque coefficient continues to diminish (Zeng et al., 2009). Lee and Balachandar (2010) investigated the torque coefficient of a rotating sphere at various particle-wall distances. They found that the torque coefficient decreases as the particle Reynolds numbers and wall distances increase. Moreover, Meng et al. (2022) found that when a spherical particle is affixed to a rough wall characterized by regularly arranged hemispherical pits, the torque coefficient of the particle increases with larger asperity sizes.

It is necessary to distinguish these wall-force studies from the distinct research paradigm that addresses particle behaviour in confined flows, which has evolved along a separate but equally important trajectory (Yu et al. 2010; Anand and Subramanian 2023). In the context of confined flows, studies have focused primarily on the migration of finite-sized particles in pipes or ducts (Segre and Silberberg 1962; Matas et al. 2004; van der Sman, 2010; Fox et al. 2021; Su et al. 2023; Lin et al. 2025). While such migration studies provide fundamental insights into lift mechanisms and particle–flow–wall interactions (Cox and Brenner 1968; Ho and Leal 1976; Chen and Jiang 2023; Lauricella et al. 2024), they generally deal with freely moving, neutrally buoyant particles rather than particles adhered to a wall. For comprehensive reviews on inertial migration and lift forces on particles in confined shear and Poiseuille flows, the reader is referred to Asmolov et al. (2018) and Shi and Rzehak (2020). Therefore, the forces and torques acting on a particle attached to a wall in confined linear shear flows remain unexplored.

Particle detachment occurs when hydrodynamic loads exceed

interfacial adhesion forces, a process governed by well-established mechanical criteria and contact models. Micro-sized particles can be detached from surfaces through three primary mechanisms: lifting, sliding, and rolling (Hubbe, 1984; Chequer et al., 2021; Hafen et al., 2023). Direct lift-off is generally less favourable due to the relatively small magnitude of the lift force compared to drag. In practice, sliding and rolling are more frequently observed (Cui and Sommerfeld, 2018; Ting et al., 2023). The dominant detachment mechanism depends on surface topography: on smooth walls, rolling tends to initiate before sliding (Cui and Sommerfeld, 2015), whereas on rough surfaces, the local asperity geometry plays a decisive role. For instance, sliding is favoured over rolling on convex asperities (Cui and Sommerfeld, 2022), whereas concave structures promote rolling initiation (Meng et al., 2022).

In conclusion, a critical synthesis reveals that while substantial knowledge exists for particle dynamics in either unconfined or migration-dominated scenarios, the intersection of confinement effects with wall detachment mechanics represents a significant knowledge gap. This gap is particularly critical because confinement fundamentally alters flow structures around particles, enhancing blockage effects, modifying stagnation points, and redistributing pressure and shear stress, thereby rendering existing unconfined flow correlations potentially inadequate for practical engineering systems where confinement is inherent.

This study directly addresses this gap by integrating Graphics Processing Unit (GPU) accelerated lattice Boltzmann simulations with theoretical analysis to achieve two primary objectives: first, to establish empirical correlations that accurately predict hydrodynamic forces and torques under confinement as functions of both particle Reynolds number and height-to-size ratio (i.e., the ratios of the gap between the upper and lower walls to the particle size); second, to develop an algorithm for determining critical detachment conditions that can be directly implemented in Eulerian-Lagrangian computational frameworks. The practical significance of this work lies in enabling accurate prediction of contaminant particle behaviour in critical engineering systems such as hydraulic components and microsensors, thereby providing designers with tools to optimize clearance geometries and operational parameters to minimize particle related failures and extend component service life. The paper is organized as follows: Section 2 details the numerical methodology and validation; Section 3 presents the effects of confinement on forces and torques coefficients; Section 4 develops empirical correlations for confined Couette flow by introducing correction factors to existing formulations; Section 5 analyses particle detachment thresholds and presents the critical-condition algorithm; and Section 6 summarizes the main conclusions.

2. Setups of the lattice Boltzmann simulation

2.1. Lattice Boltzmann method

The lattice Boltzmann method (LBM) is widely acknowledged as an efficient and robust computational fluid dynamics (CFD) technique for simulating fluid behaviour (McNamara and Zanetti, 1988; Higuera and Jiménez, 1989; He and Luo, 1997; Chen and Doolen, 1998; Chen et al., 2024). Instead of directly solving the Navier-Stokes equations, LBM simulates fluid density on a lattice by employing streaming and collision (relaxation) processes along the lattice links defined by the discrete velocity set. Each lattice node is associated with an equilibrium distribution function, and the collision and streaming operations are performed along the lattice links defined by the discrete velocity set (Bhatnagar et al., 1954). The D3Q19 model with 19 discrete velocity vectors is employed in the numerical implementation (Qian et al., 1992). The discrete LB equation with a multi-relaxation-time (MRT) collision operator is employed (d'Humières, 1994; d'Humières et al., 2002). The numerical implementation is based on the same GPU-accelerated LBM code used and validated in previous work (Meng et al., 2022; Gao et al., 2025; see the latter for details), which itself is developed from the open-source framework FluidX3D (Lehmann, 2022; Lehmann et al., 2022).

The LBM demonstrates significant efficiency in the computation of hydrodynamic forces acting on particles or clusters of particles (Yu et al., 2025; Zhang et al., 2025). The curved boundary of the particle is handled using an extrapolation scheme (Guo et al., 2002), ensuring accurate computation of hydrodynamic forces and torque via momentum exchange between fluid and solid nodes. In comparative analyses, the GPU implementation utilizing the NVIDIA GeForce RTX 3090 demonstrates simulation speeds 30 to 50 times faster than those achieved on an AMD EPYC™ 7742 processor (60 cores) with an equivalent number of grid cells.

2.2. Boundary conditions

Fig. 1 illustrates the boundary conditions employed in the LB simulation. A spherical particle is attached centrally to the bottom wall within a cuboidal computational domain. A no-slip boundary condition is applied to both walls: the top wall moves with a constant streamwise velocity U_0, while the bottom wall is stationary. This setup establishes a linear shear (Couette) flow. At the top wall, the velocity is prescribed as (U_0, 0, 0); at the bottom wall, it is (0, 0, 0). Periodic boundary conditions are applied to the side walls (with normal vectors in the x- or z-directions), simulating an infinitely extended channel. The particle Reynolds number and height-to-size ratio are defined as

$$\mathrm{Re_p} = \frac{\mathrm{G}D_p^2}{2\nu}, \kappa = H/D_\mathrm{p}, \tag{1}$$

where $G = U_0/H$ is the shear rate (with U_0 being the velocity of the top moving wall), D_p is the diameter of the particle, and ν is the kinematic viscosity of the fluid. The Re_p was varied by adjusting the U_0, while keeping the fluid properties and geometric dimensions fixed. The coefficients for drag, lift, and torque are defined as follows (Zeng et al., 2005; Fillingham et al., 2021)

$$\left.\begin{aligned} c_D &= \frac{32F_D}{\rho\pi G^2 D_p^4} = \frac{8}{\pi}\left[\int_S (-p\boldsymbol{n} + \boldsymbol{n}\cdot\tau)\mathrm{d}\mathbf{S}\right]\cdot\boldsymbol{e}_\mathbf{x}, \\ c_L &= \frac{32F_L}{\rho\pi G^2 D_p^4} = \frac{8}{\pi}\left[\int_S (-p\boldsymbol{n} + \boldsymbol{n}\cdot\tau)\mathrm{d}\mathbf{S}\right]\cdot\boldsymbol{e}_\mathbf{y}, \\ c_M &= \frac{64M_h}{\rho\pi G^2 D_p^5} = \frac{16}{\pi}\left[\int_S (\boldsymbol{r}\times\tau)\mathrm{d}\mathbf{S}\right]\cdot\boldsymbol{e}_\mathbf{z}, \end{aligned}\right\} \tag{2}$$

where F_D, F_L, M_h, p, and S denote the drag force, lift force, hydrodynamic torque acting on the particle, the static pressure on the particle's surface, and the particle's surface area, respectively. The vector variables $\boldsymbol{n}$, τ, and $\boldsymbol{r}$ represent the normal vector of the surface, the dimensionless viscous stress tensor, and the position vector from the center of the particle to a specific point on the particle's surface, respectively. Additionally, $\boldsymbol{e}_x$, $\boldsymbol{e}_y$, and $\boldsymbol{e}_z$ are the unit vectors in the streamwise, vertical, and lateral directions, respectively.

To facilitate a comprehensive analysis of the contributions of the above coefficients arising from pressure and viscous effects, the pressure coefficient c_p and the skin friction coefficient c_f are introduced (Laín et al., 2024)

$$c_p = \frac{8p}{\rho G^2 D_p^2}, c_f = \frac{8|\boldsymbol{\tau}_w|}{\rho G^2 D_p^2}, \tag{3}$$

where $|\boldsymbol{\tau}_w|$ represent the magnitude of the wall shear stress, and the definition of wall shear stress is given by

$$\boldsymbol{\tau}_w = \mu\frac{\partial u}{\partial n}, \tag{4}$$

where μ is the dynamic viscosity of the fluid.

2.3. Domain and Mesh independence study

A domain independence study is first conducted to determine the smallest domain for which top wall confinement effects on forces and torque of the wall-attached particle become negligible, enabling subsequent numerical validation against unconfined linear shear flow. The domain independence study is conducted in two sequential steps. First, the dimensions of the domain's length and width are modified while maintaining a constant height. Then, the height of the domain is adjusted while keeping the length and width constant. The length-to-width ratio of the domain is consistently maintained at 3:2, as established in the research conducted by Derksen and Larsen (2011). Given that hydrodynamic forces exhibit increased sensitivity to domain size at lower particle Reynolds numbers (Ekanayake et al., 2020), the smallest particle Reynolds number considered in this study ($Re_p = 0.1$) is employed for the domain independence study. Fig. 2 illustrates the effect of domain size on the drag, lift, and torque coefficients. The results indicate that a domain size of $24D_p \times 16D_p \times 12D_p$ (length × width × height) is sufficient for the LB simulations.

To verify the adequacy of the grid size for the LBM simulation, a particle Reynolds number of 40 is utilized, as hydrodynamic forces exhibit greater sensitivity to grid resolution at higher particle Reynolds numbers (Fillingham et al., 2021). The number of cells per particle diameter is varied from 10 to 30, with 25 cells per particle diameter determined to be sufficient for obtaining accurate force computations. The relative errors in the drag, lift, and torque coefficients are 0.029 %, 0.058 %, and 0.044 %, respectively, when compared to the results obtained with 30 cells per particle diameter. The total number of grid cells utilized in a simulation amount to 72 million, with a computational time of approximately 2 to 3 days when employing the NVIDIA GeForce RTX 3090.

2.4. Numerical validation

The scenario involving a spherical particle in contact with a smooth wall in a linear shear flow serves as a basis for numerical validation. It is noted that the fluid domain is sufficiently large to eliminate the influence of the upper moving wall. The accuracy of the LB simulation is evaluated by comparing the current simulation results with established analytical solutions (Leighton and Acrivos, 1985; Chaoui and Feuillebois, 2003) and semi-empirical correlations (Zeng et al., 2009; Lee and Balachandar, 2010; Meng et al., 2022; Gao et al., 2025). The particle Reynolds number ranges from 0.1 to 40. As illustrated in Fig. 3, the strong correlation between the results obtained from the present LB simulation and those reported in the literature further confirms the reliability of the current LB simulations. Note that for the torque coefficient in Fig. 3c, the data point from Zeng et al. (2009) is a discrete DNS result (as no correlation was provided), while in Figs. 3a and 3b, the corresponding values are derived from their empirical correlations. Moreover, Gao et al. (2025) correlate drag, lift, and torque for a wall-attached spheroid; at an aspect ratio of 1, their data match ours closely.

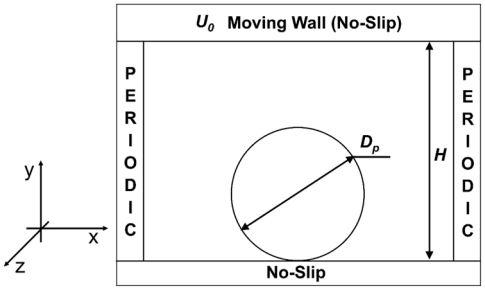


Fig. 1. Computational domain illustrating the applied boundary conditions and relevant coordinate systems.

3. Forces acting on the particle

3.1. Flow features

Fig. 4 presents flow characteristics around the particle for various particle Reynolds numbers and height-to-size ratios. Pressure coefficient contours surrounding the particle appear as coloured profiles, with magenta lines indicating isobars of c_p. The skin friction coefficient distribution on the particle surface is depicted by a colour map, with black contour lines overlaid representing isovalues of c_f. Forward and rear stagnation points (designated SP1 and SP2) are observable on the windward and leeward surfaces as labelled. Notably, streamlines, represented by arrow-headed black lines, may deviate from the $Z = 0$ plane with some passing around the particle's front or rear. Furthermore, as the particle Reynolds number increases, enhanced fluid inertial effects lead to the emergence of flow separation, resulting in the formation of recirculating vortices in the leeward region of the particle. Concurrently, a reduction in the height-to-size ratio causes the streamlines above the particle to straighten due to the constraints imposed by the wall confinement.

To better understand how the wall effect influences the streamlines around the particle, Figs. 5 and 6 are presented. Figs. 5 and 6 present three-dimensional streamlines originating from different designated starting positions in the windward region near the particle at varying particle Reynolds numbers and height-to-size ratios. These starting points employ the coordinate system established in Fig. 4. Due to the symmetry of the fluid flow about the $Z = 0$ plane around the particle, only front-facing streamlines are displayed. The trajectories in Fig. 6 maintain closer proximity to the particle surface than those in Fig. 5, with an inset providing magnified near-wall streamline details. In the insets of Figs. 5 and 6 corresponding to a particle Reynolds number of 10 and a height-to-size ratio of 6, the upper wall (shaded region) and its motion direction are indicated by black arrows. To make the upper wall visually discernible in this view, it is schematically placed at a distance of 1.5 D_p from the lower wall for illustration purposes; the actual wall-particle separation is larger and serves only as a directional reference. The colour along each streamline represents the local dimensionless velocity magnitude, defined as $U^* = 2\,U\,/\,(GD_p)$, where U is the flow velocity magnitude. In Fig. 5, the dimensionless velocity magnitude ranges from 0 to 2, whereas in Fig. 6, it spans from 0 to 1, with an inset magnifying near-wall details where the velocity varies between 0 and 0.1. Notably, streamlines become deflected away from the particle's bottom due to extremely small gap between the particle and the lower wall.

3.2. Drag coefficient

Fig. 7 illustrates the influence of the height-to-size ratio on the drag coefficient across varying particle Reynolds numbers. To accentuate variations with increasing Reynolds number, the drag coefficient is multiplied by the particle Reynolds number on the y-axis. As the particle Reynolds number rises, the quadratic growth of the velocity at the particle centre substantially outpaces the increase in hydrodynamic drag force, resulting in a decline in the drag coefficient, a trend also observed for the lift and torque coefficients in Figs. 11 and 13. Moreover, enhanced inertial effects induce flow separation accompanied by leeward recirculation as shown in Fig. 4, further reducing these coefficients. However, a decrease in the height-to-size ratio corresponds to an increase in the drag coefficient. Following Zeng et al. (2005) and Gao et al. (2025), the drag coefficient can be decomposed into pressure ($c_{D,p}$) and viscous ($c_{D,v}$) components, and the lift coefficient is decomposed likewise.

A reduction in the height-to-size ratio increases the proportion of the particle's cross-sectional area relative to the central flow passage,

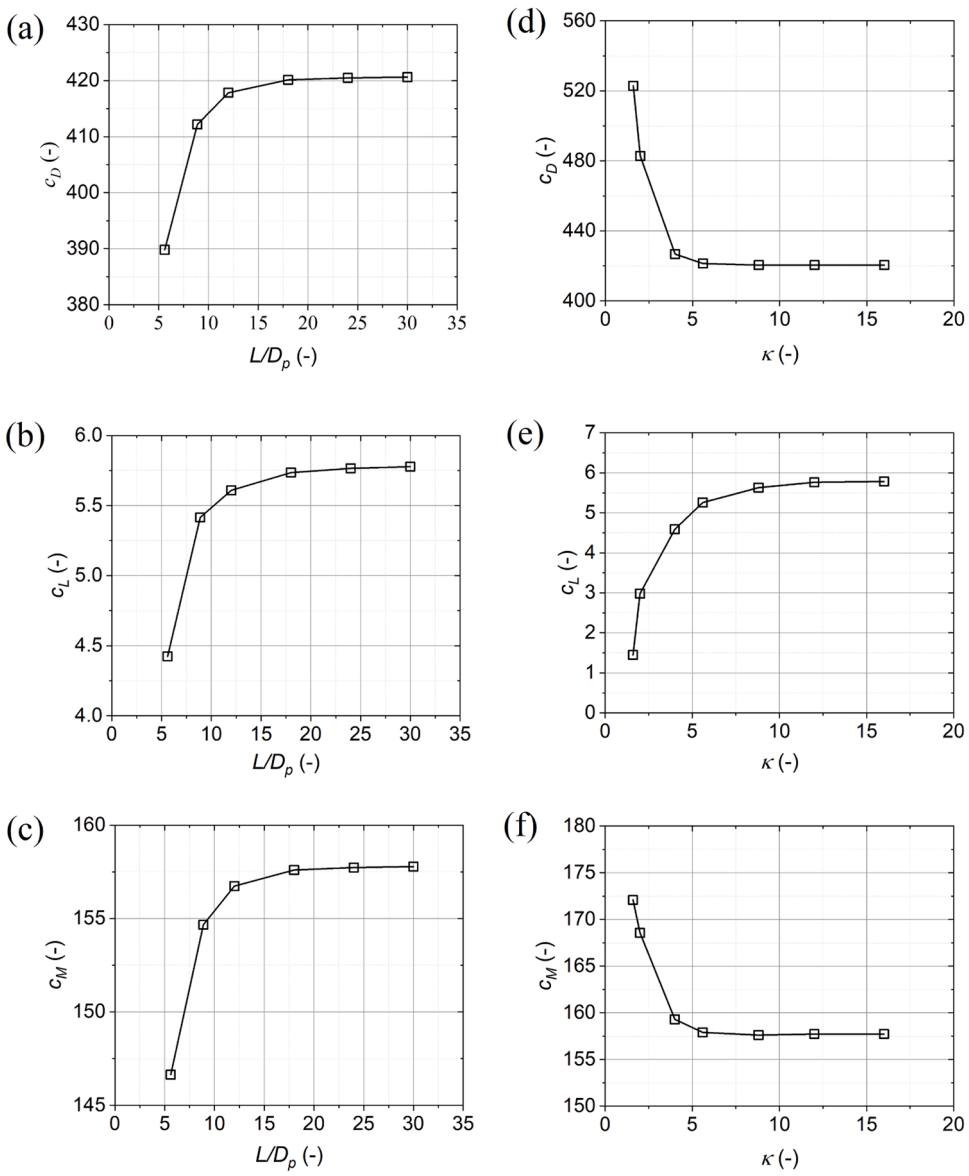


Fig. 2. The influence of fluid domain dimensions on the coefficients of drag (first row), lift (second row), and torque (third row). The left column depicts the variation in domain length (L) while maintaining a constant height (H) of $6D_p$. Conversely, the right column illustrates the variation in domain height while keeping the domain length constant at $24D_p$. In all scenarios, the ratio of domain length to domain width (W) is held constant at $L{:}W = 3{:}2$, and the particle Reynolds number is consistently set at 0.1.

thereby intensifying the particle blockage effect. Enhanced wall confinement also deflects streamlines downward toward the lower wall, as shown in Figs. 5 and 6. In Fig. 5, streamlines originating at $L_z = 0.5$ and $L_z = 0.625$ deviate noticeably from the $Z = 0$ plane, while in Fig. 6, all four streamlines from $L_z = 0.5$ wrap around the lower hemisphere of the particle. This downward redistribution of flow, consistent with momentum conservation, decelerates the upstream streamwise velocity at smaller height-to-size ratios, as supported by the dimensionless velocity profiles in the Fig. 8 inset. These profiles are taken along Line A, located one particle diameter upstream of the particle (see Fig. 4), with dimensionless velocities defined as $U_x^* = 2U_x/(GD_p)$ and $U_y^* = 2U_y/(GD_p)$, where U_x and U_y are the streamwise and vertical velocity components, respectively.

However, due to the increased blocking effect of the particle, the streamwise velocity above the particle increases, as shown in Fig. 8. This flow acceleration leads to a pressure rise on the upstream side of the particle at lower height-to-size ratios, as shown by the pressure coefficient profiles in Fig. 9. These profiles are plotted along the dimensionless streamwise position L_x (defined in Fig. 4), where $L_x = -0.5$ corresponds to the upstream end and $L_x = 0.5$ to the downstream end of the particle. The constricted flow area in the central region accelerates the fluid past the particle, causing the pressure coefficient on the downstream side to decrease further at smaller height-to-size ratios. Although wall confinement shifts both the front (SP1) and rear (SP2) stagnation points upward, redistributing pressure toward the upper region and partially offsetting the pressure drag, the overall pressure amplitude is the dominant factor. As a result, the pressure drag coefficient increases significantly at reduced height-to-size ratios due to the amplified pressure difference between the upstream and downstream sides of the particle.

The viscous drag coefficient also increases with decreasing height-to-size ratios due to elevated shear rates near the particle's upper surface, as shown in Fig. 8, where flow acceleration occurs in the constricted central region. Since the peak shear stress position remains stable, its influence on viscous drag coefficient is negligible, as further illustrated in Fig. 9. The skin friction coefficient exhibits a similar increasing trend

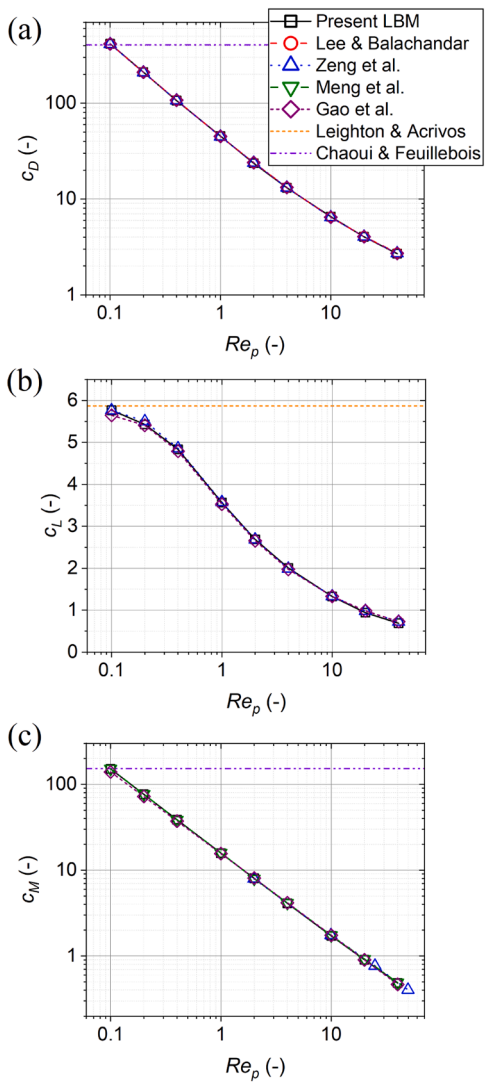


Fig. 3. The influence of the particle Reynolds number on the coefficients of drag (a), lift (b), and torque (c) for a particle adhered to a flat surface in unconfined Couette flow. The simulation domain dimensions are $24D_p \times 16D_p \times 12D_p$ (length × width × height), with a grid resolution of 25 cells per particle diameter.

across particle Reynolds numbers from 0.1 to 10. Overall, both pressure and viscous drag components grow with reduced height-to-size ratios, leading to a total drag coefficient increase of up to 24.4 % when the ratio decreases from 12 to 1.5.

The viscous drag contributes more significantly to the total drag than the pressure component, as shown in Fig. 10, though its influence diminishes with increasing particle Reynolds number. Enhanced inertial effects intensify flow separation, as visible in the streamlined detachment at $Re_p = 10$ compared to $Re_p \leq 1$ in Fig. 6, while boundary layer thinning further reduces shear stress and viscous drag. The effect of height-to-size ratio on drag becomes negligible when $\kappa > 6$. Increasing κ from 6 to 12 changes the drag coefficient by less than 0.21 %, a result consistent with the overlapping velocity profiles for $\kappa = 6$ and 12 in Fig. 8.

3.3. Lift coefficient

The lift coefficient decreases with a reduced height-to-size ratio, as shown in Fig. 11. Fig. 12 shows the ratio of each component to the total lift across different height-to-size ratios and particle Reynolds numbers. At $Re_p \leq 1$, the pressure lift exceeds the viscous component when $\kappa \leq 2$, but falls below it when $\kappa \geq 4$. This occurs because wall confinement strongly suppresses vertical flow near the upper wall, sharply reducing viscous lift. Although pressure lift also decreases, its decline is less pronounced, leading to its increased relative contribution. In contrast, at $Re_p = 10$, pressure lift consistently dominates across all κ values. This aligns with stronger inertial effects at higher Reynolds numbers, where flow separation and leeward recirculation (Fig. 4) break pressure symmetry, significantly raising the pressure lift component and making it dominant in the total lift.

As the height-to-size ratio decreases, both pressure and viscous lift coefficients decline, leading to a reduction in the total lift coefficient. Specifically, the lift coefficient falls by 74 % as the height-to-size ratio decreases from 12 to 1.5. The pressure lift coefficient also decreases with increasing particle Reynolds number, as shown in Fig. 4. For instance, at $\kappa = 1.5$, the minimum pressure coefficient near the particle top rises from −145.8 to −3.3 as Re_p increases from 0.1 to 10. Moreover, the zero isobar shifts slightly downstream with decreasing κ, as visible in Fig. 4 at $Re_p = 1$, resulting in a more symmetric pressure distribution and better flow alignment, both contributing to the decrease in pressure lift. Although wall induced flow deceleration on the lower hemisphere (see Fig. 8) raises local pressure (see Fig. 4) and slightly favours lift, this effect is outweighed by the strong increase in positive pressure amplitude and its upward shift on the upper hemisphere. Consequently, the net pressure difference between the upper and lower hemispheres decreases, driving the overall reduction in pressure lift with smaller height to size ratios.

The viscous lift coefficient varies primarily due to changes in streamline direction at different height-to-size ratios, as shown in Figs. 5 and 6. Under strong confinement (low κ), the vertical velocity component (U_y^*) is suppressed, reducing viscous lift. For $\kappa > 6$, velocity differences become negligible at finite Reynolds numbers; for example, at $Re_p = 10$, increasing κ from 6 to 12 changes the viscous lift coefficient by less than 0.22 %. In contrast, at low Reynolds numbers ($Re_p \leq 1$), the same change in κ leads to a significant difference of about 8.79 % in viscous lift. The lift force, being much smaller than drag, is more sensitive to domain dimensions, especially in viscosity-dominated flows.

3.4. Torque coefficient

Fig. 13 illustrates the influence of the height-to-size ratio on the torque coefficient across varying particle Reynolds numbers. To accentuate variations with increasing Reynolds number, the torque coefficient is multiplied by the particle Reynolds number on the y-axis. The hydrodynamic torque acting on the particle is obtained by integrating the shear stress over its surface and is closely associated with viscous effects. As the height-to-size ratio decreases, the acceleration of flow around the particle under constrained conditions leads to an elevated shear rate near the surface, thereby increasing the torque coefficient. Specifically, when the ratio decreases from 12 to 1.5, the torque coefficient rises by up to 5.85 %.

A more detailed analysis shows that the reduced flow velocity beneath the particle lowers local shear stress, which contributes positively to the overall torque by enhancing the asymmetry of shear distribution. This effect, combined with the significantly increased shear on the upper surface, results in a net increase in torque coefficient. Notably, when the height to size ratio exceeds 6, the torque coefficient exhibits only minor variations, a trend consistent with the behaviour observed for the drag coefficient, further indicating the weakening of wall effects beyond this threshold.

4. Empirical correlations

From the user's perspective, in order to directly obtain the drag, lift, and torque coefficients for various particle Reynolds numbers and height-to-size ratios, it is necessary to fit the numerical simulation

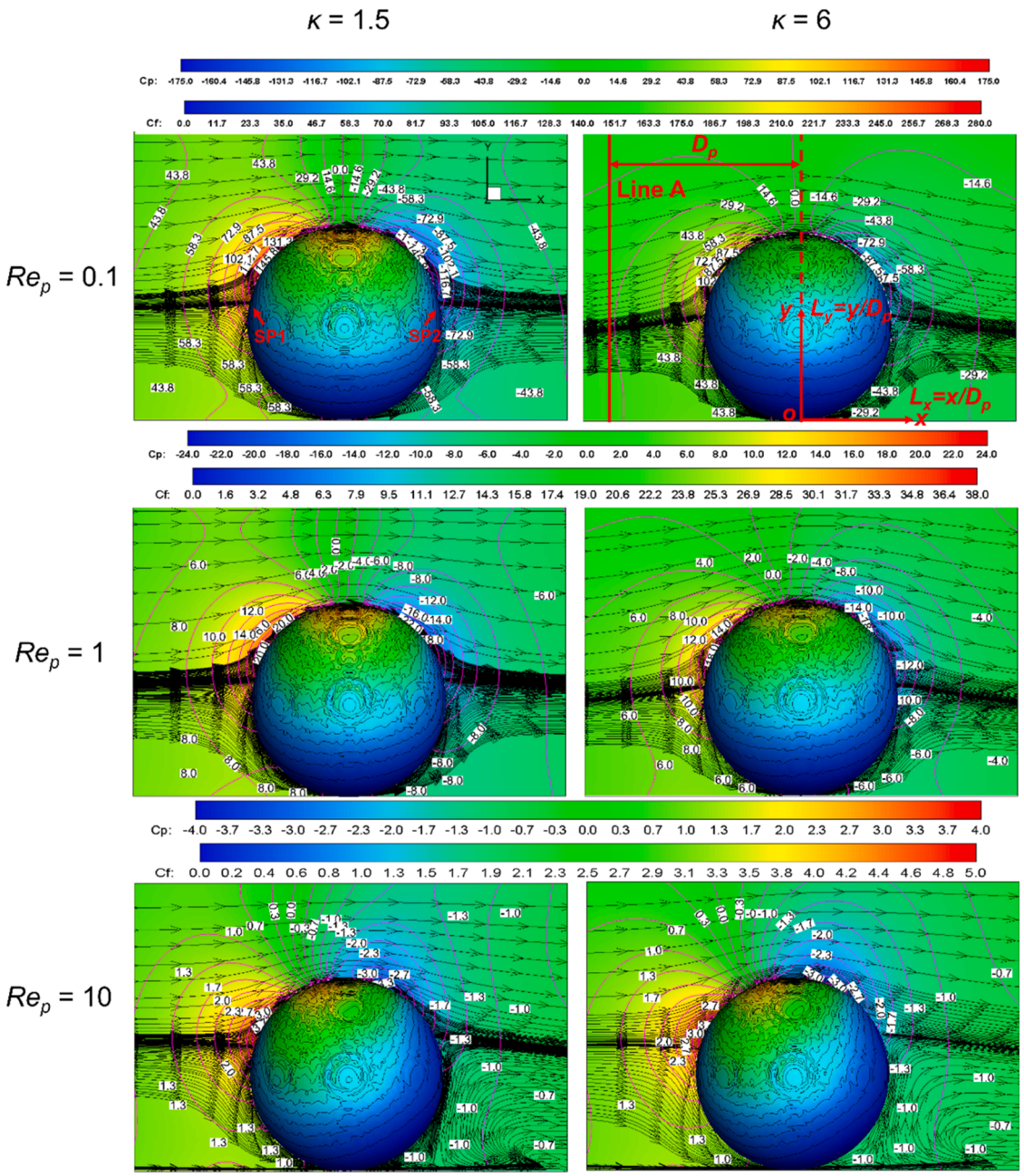


Fig. 4. Illustration of the pressure coefficient flow field near the particle at the central cross-section and the skin friction coefficient distribution on the particle surface for various particle Reynolds numbers and height-to-size ratios. All panels have a length of $2.25D_p$ and a height of $1.5D_p$, with black lines indicating the streamlines.

results from Figs. 7, 11 and 13. Subsequently, these empirical correlations can be used in study of particle detachment and further employed to determine the critical particle Reynolds number at the initial of detachment. To ensure the empirical correlations are as simple as possible, highly accurate, and reliable, the existing correlations are modified through the incorporation of correction factors.

4.1. Drag coefficient

Goldman et al. (1967) and O'Neill (1968) first derived the exact Stokes solution for a sphere attached to a smooth wall

$$c_D(Re_p) = 1.7009\frac{24}{Re_p}. \tag{5}$$

To account for inertial effects in unconfined flows, Schiller & Naumann (1933) proposed the widely used semi-empirical correlation

$$c_D(Re_p) = \frac{24}{Re_p}\left[1 + 0.15Re_p^{0.687}\right], \tag{6}$$

where the expression is valid for particle Reynolds numbers less than 1000. Based on Eqs. (5) and (6), Zeng et al. (2009) and Cui & Sommerfeld (2015) combined the wall-correction factor 1.7009 with the Schiller-Naumann term to obtain a universal correlation for a wall-attached particle

$$c_D(Re_p) = 1.7009\frac{24}{Re_p}\left[1 + 0.15Re_p^{0.687}\right], \tag{7}$$

where the expression is also valid for particle Reynolds numbers less

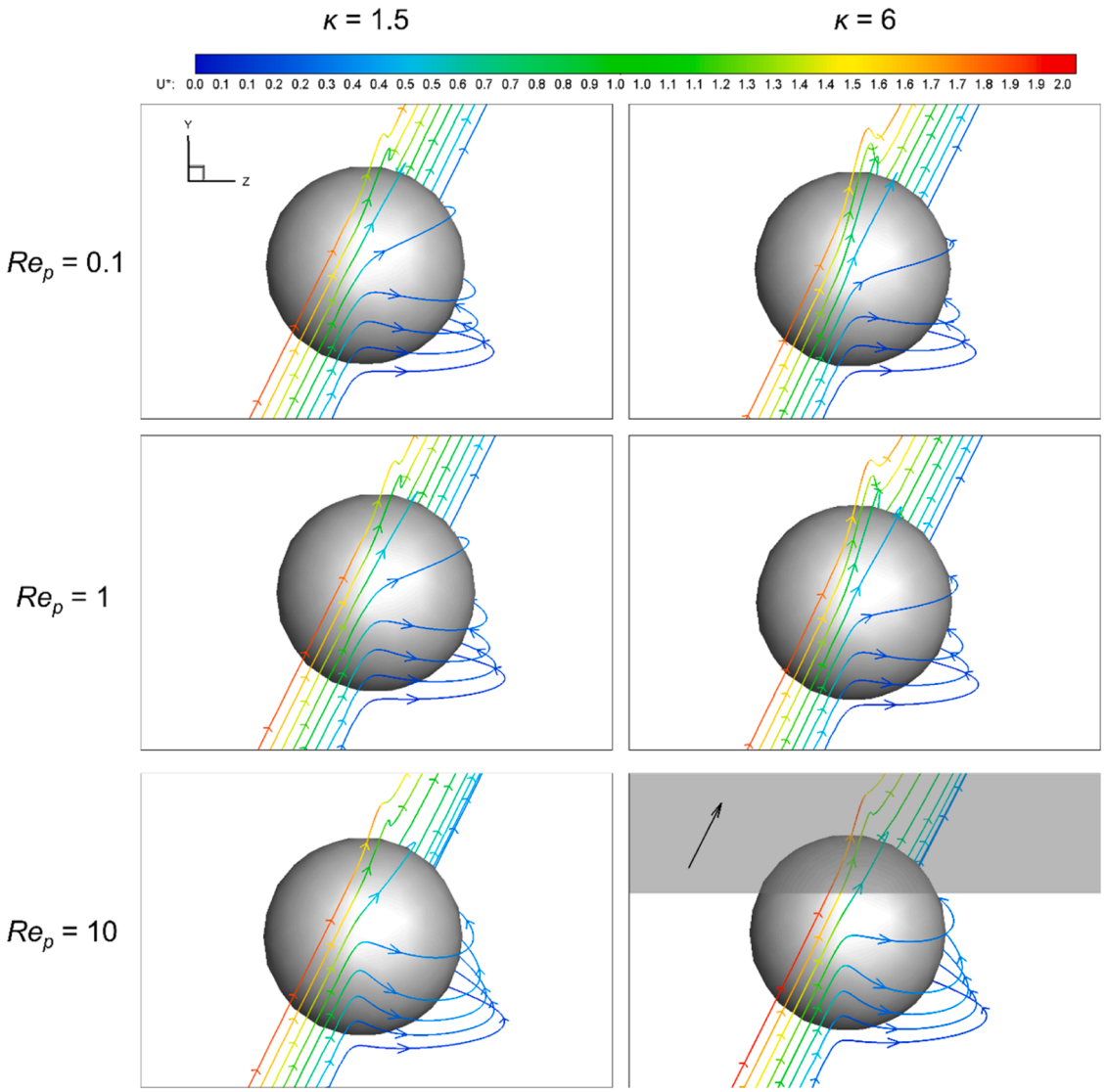


Fig. 5. Three-dimensional fluid trajectories around a sphere held fixed in a shear flow are shown for various particle Reynolds numbers and height-to-size ratios. The fluid trajectories start at points with coordinates $L_x = -1$, $L_y = 0.05$ and $L_z = 0.125 - 1$ (in increments of 0.125). All panels have a length of $2.25D_p$ and a height of $1.5D_p$.

than 1000. This unified correlation maintains the analytical solution at low particle Reynolds numbers and extends its applicability to finite particle Reynolds numbers. However, the correlation exhibits deviations in predicting wall effect influences on the drag coefficient. Therefore, Zeng et al. (2009) further proposed a more precise empirical correlation

$$c_D(Re_p) = 1.7009\frac{24}{Re_p}\left[1 + 0.104{Re_p}^{0.753}\right]. \tag{8}$$

Inspired by the evolution of the drag coefficient correlation, a correction term has been incorporated into Eq. (8) to account for the drag coefficient of a finite-sized sphere attached to a wall in a confined Couette flow.

$$\begin{aligned} c_D(Re_p,\kappa) &= 1.7009\frac{24}{Re_p}\left[1 + 0.104{Re_p}^{0.753}\right]\left[\frac{a_1 + b_1{Re_p}^{C_1}}{Re_p}\right] \\ &= 1.7009\frac{24}{Re_p^2}\left[1 + 0.104{Re_p}^{0.753}\right]\left[a_1 + b_1{Re_p}^{C_1}\right], \end{aligned} \tag{9}$$

where the coefficients a_1, b_1, and c_1 are functions of the height-to-size ratio, which can be expressed as follows

$$\left.\begin{aligned} a_1(\kappa) &= -4.096\exp(-4.159\kappa), \\ b_1(\kappa) &= 1 + 0.004\exp\left(5.595\kappa^{-0.771}\right), \\ c_1(\kappa) &= 1 - 0.061\kappa^{-1.548}. \end{aligned}\right\} \tag{10}$$

The mean relative error for the correlation of the drag coefficients is 0.94 %, while the coefficient of determination is 0.99. The lines connecting the symbols in Fig. 7 represent the fitting curves derived from Eqs. (9) and (10). It is worth noting that when the height-to-size ratio tends to infinity, that is, when the particle is influenced only by a single wall, the expression can be simplified to Equations (8). In addition, as the particle Reynolds number increases, the value of the correction term gradually decreases. This implies that the influence of the wall effect on the drag coefficient of the particle also diminishes, which is consistent with the findings of this study.

4.2. Lift coefficient

In the Stokes flow regime, the analytical solution given by Leighton and Acrivos (1985) results in a constant lift coefficient c_L of 5.87. As inertial effects become more pronounced, the numerical simulations conducted by Zeng et al. (2009) demonstrate a significant reduction in

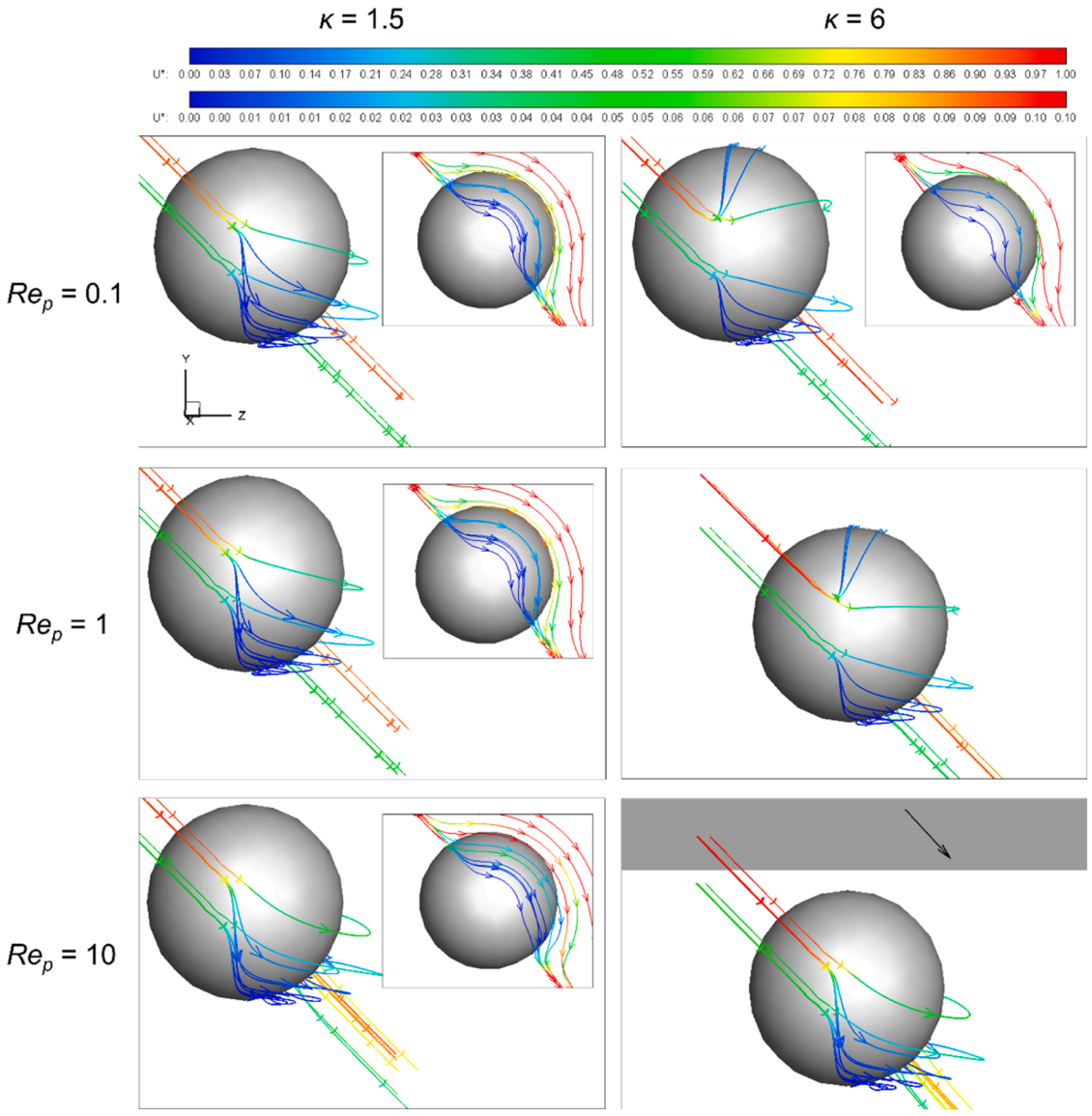


Fig. 6. Three-dimensional fluid trajectories around a sphere held fixed in a shear flow are shown for various particle Reynolds numbers and height-to-size ratios and the inset magnifies the streamlines beneath the sphere. The fluid trajectories start at points with coordinates $L_x = -1$ for (i) $L_z = 0.25$ with $L_y = 0.1$, 0.01, 0.001, 0.0001 and 0.00001, and (ii) $L_z = 0.5$ with $L_y = 0.1$, 0.01, 0.001 and 0.0001. All panels have a length of $2.25D_p$ and a height of $1.5D_p$.

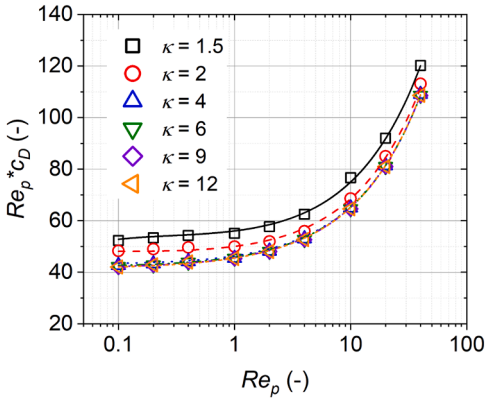


Fig. 7. The influence of the height-to-size ratio on the drag coefficients across different particle Reynolds numbers.

the lift coefficient, which can be described by the following simple expression

$$c_L(Re_p >> 1) = \frac{3.663}{Re_p^{0.44}}. \tag{11}$$

Based on this expression, Zeng et al. (2009) further established a more precise empirical correlation for the lift coefficient of a spherical particle attached to a wall in a shear flow

$$c_L(Re_p) = \frac{3.663}{\left[Re_p^2 + 0.1173\right]^{0.22}}, \tag{12}$$

where the expression is also valid for particle Reynolds numbers less than 250. Notably, the expression asymptotically approaches $c_L = 5.87$ as the particle Reynolds number tends to zero, with its validity thoroughly confirmed by multiple independent studies (Xie et al., 2018; Bhagat and Goswami, 2022; Ouchene, 2025).

Consequently, similar to the establishment of the empirical correlation for the drag coefficient, a correction factor for the lift coefficient in

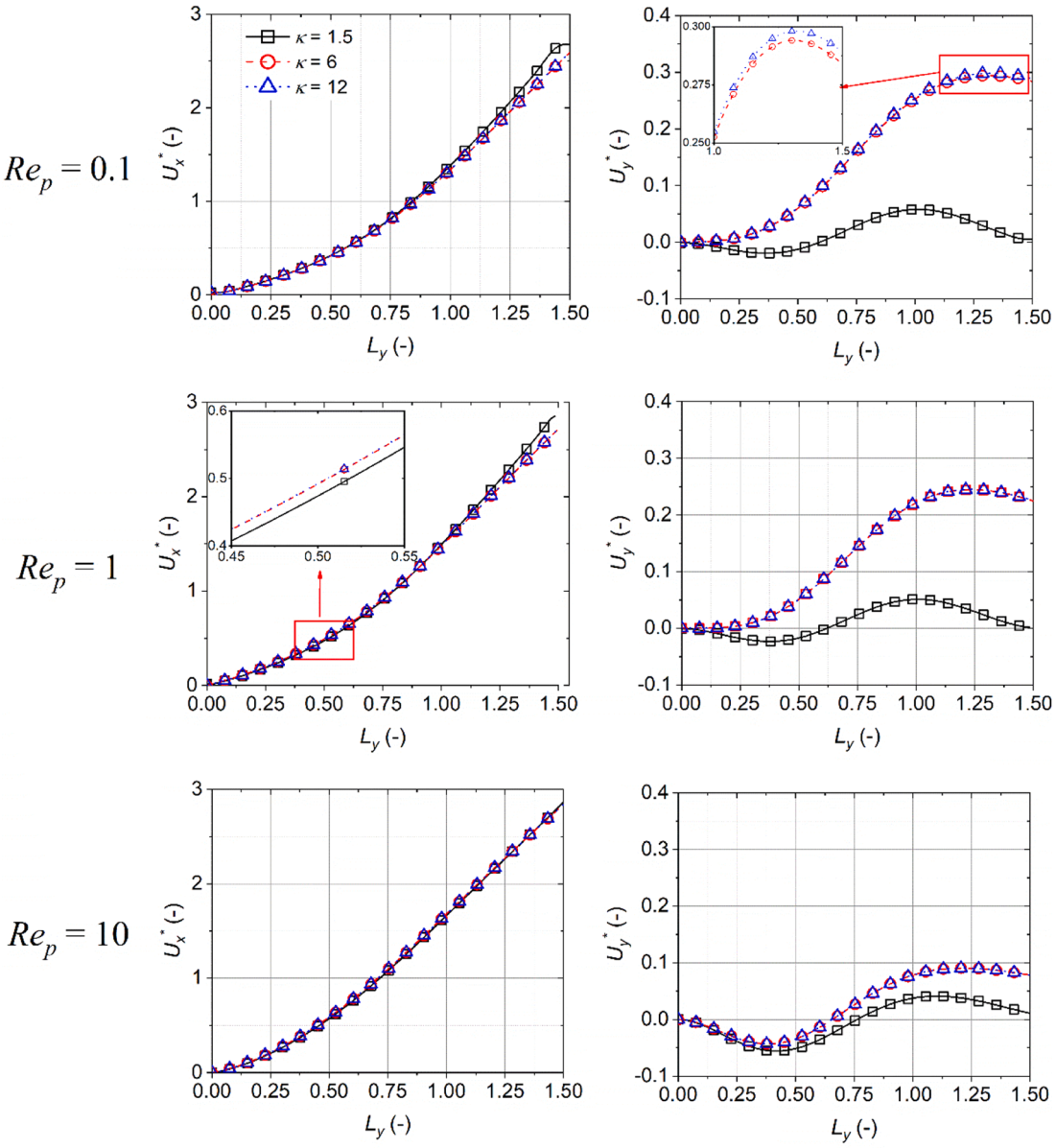


Fig. 8. The dimensionless flow velocity profiles in the streamwise (U_x*) and vertical (U_y*) directions are presented as a function of the dimensionless vertical position (L_y) for various particle Reynolds numbers. As illustrated in Fig. 4, the bottom of the particle corresponds to $L_y = 0$, while the top of the particle corresponds to $L_y = 1$. The velocity profiles are extracted from Line *A* as illustrated in Fig. 4.

confined Couette flow is introduced based on Eqs. (12)

$$c_L(Re_p) = \frac{3.663}{\left[Re_p^2 + 0.1173a_2\right]^{0.22}}, \tag{13}$$

where the coefficient a_2 is a function of the height-to-size ratio and can be expressed as

$$a_2(\kappa) = 1 + (31.921\kappa + 41.660)/(\kappa - 0.858)^4. \tag{14}$$

The mean relative error for the correlation of the lift coefficients is 2.30 %, while the coefficient of determination is 0.99. The lines connecting the symbols in Fig. 11 represent the fitting curves derived from Eqs. (13) and (14). It is worth noting that when the height-to-size ratio tends to infinity, that is, when the particle is influenced only by the lower wall, the expression can be simplified to Eq. (12).

4.3. Torque coefficient

However, analytical solutions and empirical correlations for the torque coefficient remain limited in the literature. Goldman's classical Stokes solution value of 0.37, defined as $c_M = M_h / (0.5F_D D_p)$, is incompatible with the dimensionless definition in this work (Eq. (2)) and thus not applicable to this study. While Chaoui & Feuillebois (2003) obtained a numerical value of 151.859 for torque coefficient, this result remains confined to creeping flow regimes ($Re_p \to 0$). Although Zeng et al. (2009) expanded the investigated Reynolds-number range to $2 \leq Re_p \leq 250$ via direct numerical simulations, their work did not provide an empirical correlation for torque coefficient. Recently, Gao et al. (2025) proposed a high-precision empirical correlation for wall-attached ellipsoids in shear flow, when the aspect ratio approaches unity, which can be simplified to the following simple expression

$$c_M(Re_p) = \frac{15.595}{Re_p^{0.952}}. \tag{15}$$

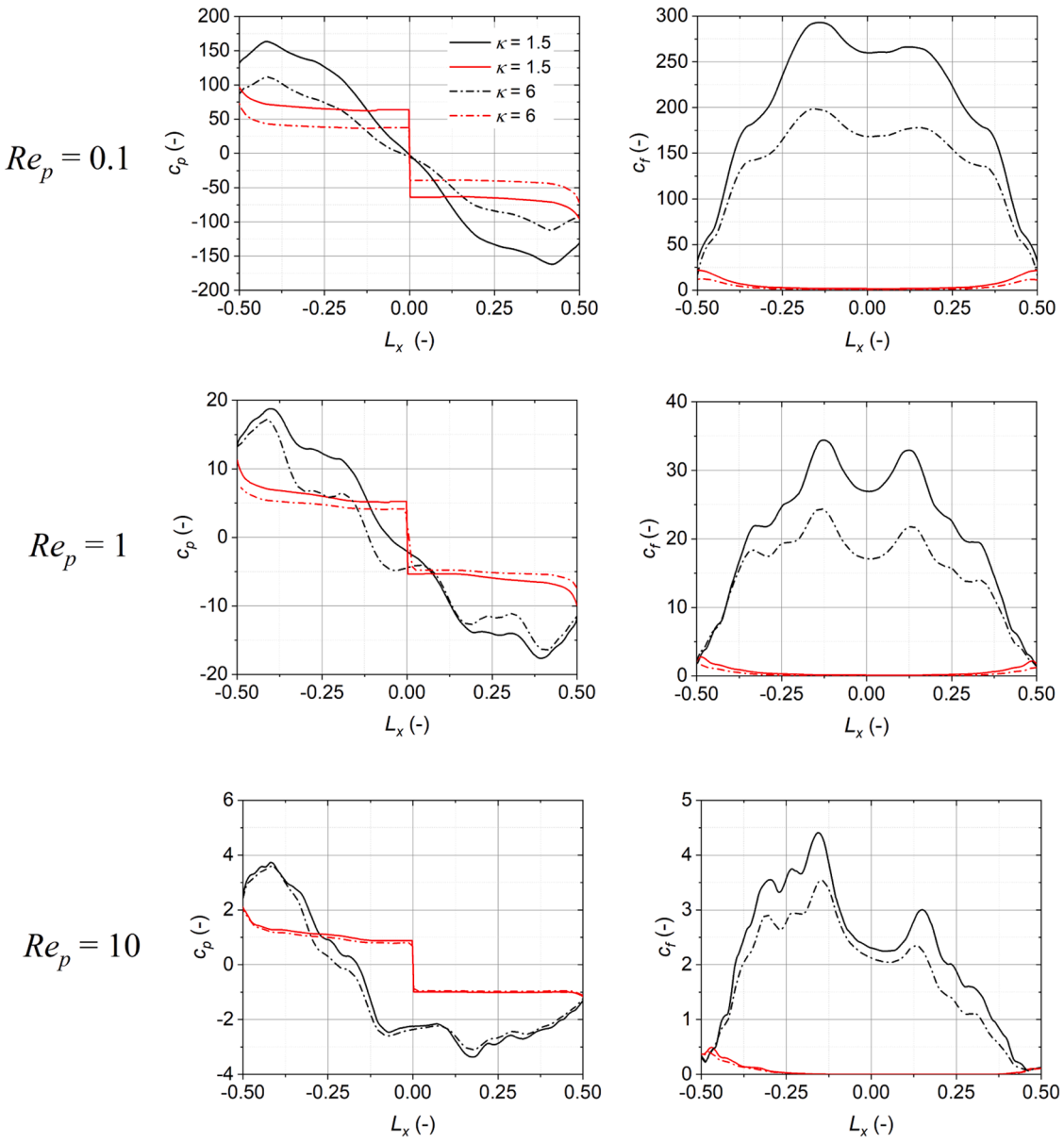


Fig. 9. The instantaneous representation of the pressure coefficient (left column) and the skin friction coefficient (right column) profiles at the midpoint of the lateral dimension of the particle is presented as a function of the dimensionless streamwise position (L_x) for various height-to-size ratios and particle Reynolds numbers. The black and red lines indicate the coefficients corresponding to the upper and lower sections of the particle surface, respectively.

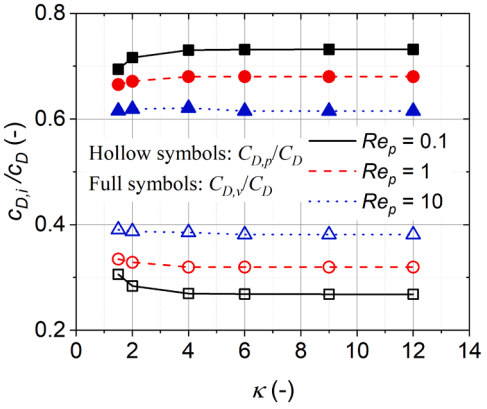


Fig. 10. The influence of the particle Reynolds number on the ratio of pressure and viscous drag coefficients to the total drag coefficient.

Notably, at $Re_p = 0.1$, the current result shows a relative deviation of approximately 0.53 % compared to Chaoui & Feuillebois (2003), while the result of Gao et al. (2025) exhibits a relative deviation of approximately 8.05 %. However, since the mean relative error between the empirical results of Gao et al. (2025) and the current numerical simulation results is about 2.84 %, a correction factor is incorporated into their existing empirical correlation to improve the prediction of the torque coefficient in confined Couette flow.

$$c_M(Re_p) = \frac{15.595}{Re_p^{0.952}}\left(\frac{a_3 + b_2 Re_p^{0.711}}{Re_p^{0.034}}\right) = \frac{15.595\left(a_3 + b_2 Re_p^{0.711}\right)}{Re_p^{0.986}}, \tag{16}$$

where the coefficient a_3 and b_2 are functions of the height-to-size ratio and can be expressed as follows

$$\left.\begin{aligned} a_3(\kappa) &= 0.998 + 0.194/\kappa^{2.939} \\ b_2(\kappa) &= 0.013 + 0.003/\kappa^{2.960} \end{aligned}\right\}. \tag{17}$$

The mean relative error for the correlation of the torque coefficients

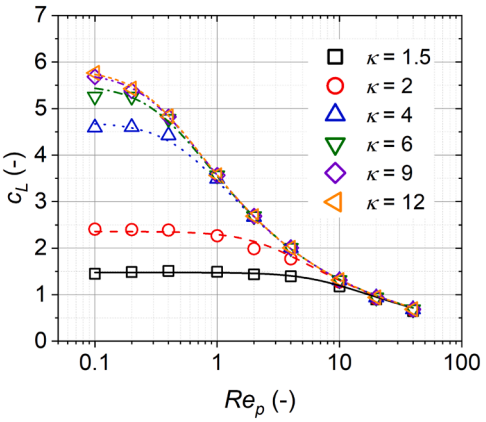


Fig. 11. The influence of the height-to-size ratio on the lift coefficient across different particle Reynolds numbers.

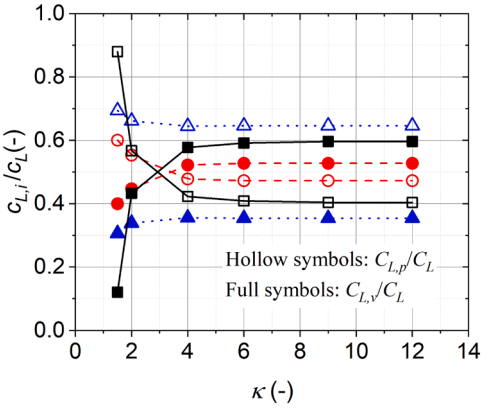


Fig. 12. The influence of the particle Reynolds number on the ratio of pressure and viscous lift coefficients to the total lift coefficient.

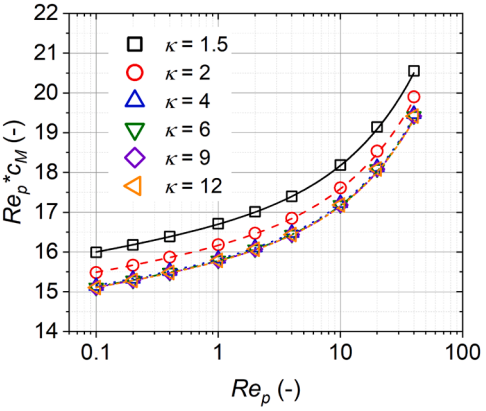


Fig. 13. The influence of the height-to-size ratio on the torque coefficient across different particle Reynolds numbers.

is 0.15 %, while the coefficient of determination is 0.99. The lines connecting the symbols in Fig. 13 represent the fitting curves derived from Eqs. (16) and (17). Similarly, when the height-to-size ratio tends to infinity, the expression can be simplified to the following simple expression

$$c_M(Re_p) = \frac{15.564 + 0.203Re_p^{0.711}}{Re_p^{0.986}}. \tag{18}$$

The correlation accurately describes the torque coefficient for a spherical particle attached to a wall in shear flow across a range of particle Reynolds numbers. For instance, at a particle Reynolds number of 0.1, the relative error compared to Chaoui & Feuillebois (2003) is just 0.51 %.

Fig. 14 shows the drag, lift, and torque coefficients as functions of the height-to-size ratio for three particle Reynolds numbers. The fitted curves, based on Equations (9) – (10) for (a), (13) – (14) for (b), and (16) – (17) for (c), agree well with the data, confirming the accuracy of the proposed correlations at a fixed Reynolds number over varying height-to-size ratios. Valid for Reynolds numbers up to 40 and height-to-size ratios from 1.5 upward, these correlations enable accurate prediction of forces and torques acting on the particle in confined Couette flow, supporting controlled particle detachment. They are useful in hydraulic and microfluidic applications (Ye et al., 2003; Tang et al., 2008; Yin et al., 2017; Sommerfeld and Taborda, 2024; Estepa-Cantero et al., 2025) for estimating contaminant release, improving removal efficiency and lifespan. Incorporated into Eulerian-Lagrangian frameworks, they enhance detachment prediction accuracy.

5. Particle detachment study

5.1. Adhesion model

The detachment of a particle from a wall can occur through three distinct mechanisms: lifting, sliding, or rolling. Fig. 15 presents a schematic diagram that helps analyse particle detachment. The particle is adhered to the wall with a contact radius (a) and an adhesion force (F_{ad}), which are governed by the contact mechanics at the interface. These quantities are typically evaluated using adhesion models, most notably the Derjaguin-Muller-Toporov (DMT) or Johnson-Kendall-Roberts (JKR) models (Derjaguin et al., 1975; Johnson et al., 1971), and the appropriate model for a given scenario can be determined using the Tabor parameter (Tabor, 1977), which distinguishes between smaller-deformation (DMT) and larger-deformation (JKR) contacts (Prokopovich and Perni, 2011). The forces acting on the particle include the hydrodynamic drag and lift, in addition to F_{ad}. For micro-sized particles, gravity force is significantly smaller than the hydrodynamic forces and is therefore considered negligible (Cui et al., 2015; Novak et al., 2023; Gao et al., 2025). Hydrodynamic torque acts about the particle's centroid. The analysis focuses on the initial detachment stage because adhesion forces diminish significantly once detachment begins, leading to subsequent motion via rolling, sliding, or lifting driven by hydrodynamic forces (Gao et al., 2025).

When the lift force exceeds the adhesion force, the particle can be detached from the surface through the mechanism of lifting. Similarly, if the drag force exceeds the frictional force, the particle can be removed via sliding. Rolling detachment occurs at a specific location, designated as point X. At this point, if the torque generated by the hydrodynamic torque and the drag force exceeds the torque produced by the adhesion and lift forces, rolling detachment will occur. The criteria for detachment through lifting, sliding, and rolling are summarized as follows

$$\left.\begin{array}{l}\text{Lifting}: F_L \geq F_{ad},\\ \text{Sliding}: F_D \geq \mu P,\\ \text{Rolling}: M_h + 0.5F_D D_p \geq aP,\end{array}\right\} \tag{19}$$

where μ, taken as 0.11 (Gao et al., 2025) due to the lubrication provided by the hydraulic oil, denotes the coefficient of friction as defined by Coulomb's law; $P = F_{ad} - F_L$ represents the effective normal force; and a is the contact radius, whose determination is related to the contact model adopted. It is noted that the contact radius is significantly smaller than the particle diameter, resulting in its exclusion from the torque component generated by the drag force. The adhesive force can be calculated using either the DMT model or the JKR model. The appropriate model for a specific problem can be determined by applying the Tabor parameter, λ, as introduced by Tabor (1977)

$$\lambda = \left[\frac{32 D_p W_A^2}{9 E_c^2 D_0^3}\right]^{\frac{1}{3}}, \tag{20}$$

Where W_A, E_c, and D_0 denote the surface energy, the composite Young's modulus, and the typical atomic distance of the particle material, respectively. The composite Young's modulus can be determined by

$$E_c = \frac{2E}{3 - 3\sigma^2}, \tag{21}$$

where σ represents Poisson's ratio, and E denotes Young's modulus.

In the context of the JKR model, the adhesion force acting on the particle, as well as the contact radius of the particle, can be evaluated by

$$F_{ad} = \frac{3}{2}\pi W_A D_p. \tag{22}$$

$$a = \left[\frac{3\pi W_A D_p^2}{E_c}\right]^{\frac{1}{3}}. \tag{23}$$

This study investigates the detachment of pollutant particles from the surfaces of hydraulic components, which are primarily composed of stainless steel. The pollutant particles present in hydraulic oil typically exhibit material properties similar to those of the hydraulic components, as they primarily originate from the erosion of the metal due to cavitation phenomena. Table I summarizes the material properties of both the stainless steel and the hydraulic oil used in this detachment study (Gao et al., 2025). The JKR model is applicable when λ is much greater than 1, while the DMT model is suitable for scenarios where λ is much less than 1. (Tabor, 1977; Fillingham et al., 2019). In this study, the Tabor parameter ranges from 9.66 to 11.72. All values in this range are much greater than 1, which firmly satisfies the criterion for applying the JKR model to determine the adhesion force and contact radius. As indicated in Table I, the contact radius ranges from 1.36 μm to 1.65 μm, while the adhesion force varies from 0.3532 mN to 0.6359 mN. The dimensionless adhesion force is defined as

$$F_{ad}^* = \frac{\rho_f F_{ad}}{\nu G D_p^2}. \tag{24}$$

To examine the tendency for particle detachment, the lifting, sliding, and rolling ratios are further defined (denoted as φ_{lift}, φ_{slide}, and φ_{roll}) as the quotient of the left-hand components divided by the right-hand components of Eq. (9). These ratios are defined as follows

$$\left.\begin{aligned} &\text{Lifting}: \varphi_{lift} = F_L / F_{ad}, \\ &\text{Sliding}: \varphi_{slide} = F_D / [\mu P], \\ &\text{Rolling}: \varphi_{roll} = \left[M_h + 0.5 F_D D_p\right] / [aP]. \end{aligned}\right\} \tag{25}$$

Notably, by setting these ratios to 1, the critical particle Reynolds number ($Re_{p,cri}$) required for initial particle detachment can be inversely solved. Moreover, if the material combination (e.g., rigid vs elastic contact) or the fluid environment (e.g., polar media like water) differs from our setup, the appropriate contact model and the dominant adhesion mechanism would change substantially. A significantly lower λ would favour the DMT model, whereas the emergence of dominant capillary forces would render both DMT and JKR models insufficient, necessitating approaches such as Lifshitz theory or capillary-adjusted JKR extensions (Rosa et al., 2008; Kosaku et al., 2023).

5.2. Results analysis

Fig. 16 presents a phase diagram relating the height-to-size ratio to the critical particle Reynolds number under varying adhesion forces in confined Couette flow. The blue, red solid, red dashed, and black curves represent the critical boundaries for rolling, sliding ($\mu = 0.11$), sliding ($\mu = 0.22$), and lifting detachment, respectively. Regions A, R, S, and L correspond to adhesion, rolling, sliding, and lifting states. The lifting boundary (black curve) is computed under the assumption of a fixed and stationary particle. In practice, if rolling or sliding occurs at lower Re_p, additional lift mechanisms, such as Magnus lift induced by rolling (Lee and Balachandar, 2010) or wall-induced lift due to sliding (Zeng et al., 2005), may emerge and alter the actual lift-off condition, which is beyond the scope of this study. At low particle Reynolds numbers, hydrodynamic forces are insufficient to overcome adhesion, resulting in the adhesion region (A) occupying the left portion of the diagram.

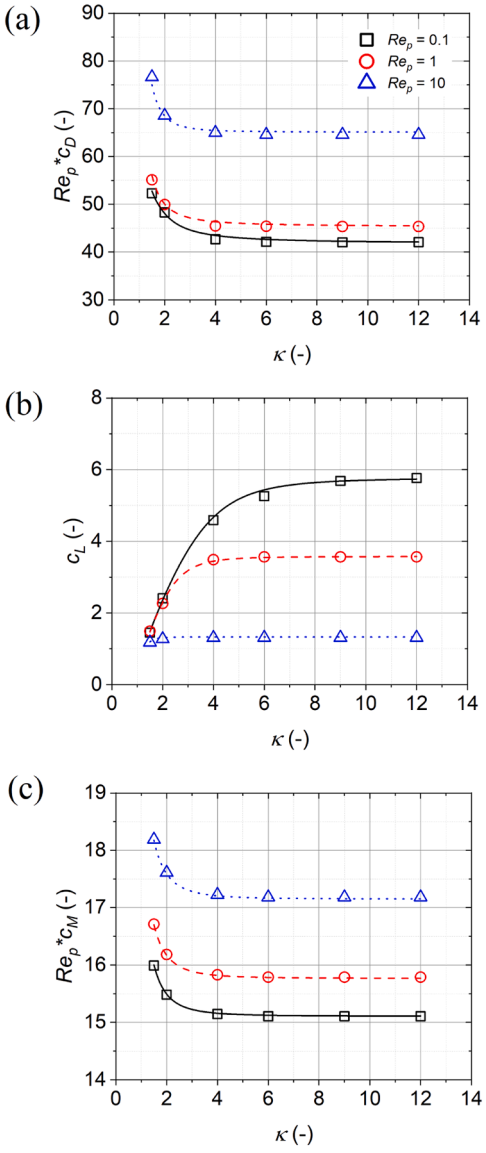


Fig. 14. The influence of the particle Reynolds number on the drag, lift and torque coefficients across various height-to-size ratios.

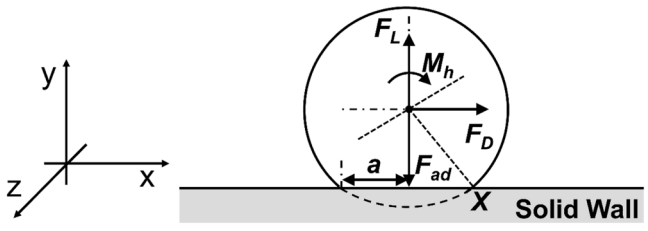


Fig. 15. A spherical particle attached to a wall with contact area and relevant forces.

Lifting detachment is the most difficult to initiate, as lift forces remain significantly smaller than drag throughout the studied Reynolds number range. The $Re_{p,cri}$ for lifting is approximately 30, where wall effects on lift attenuation are negligible. As a result, the lift force varies insignificantly with the height-to-size ratio, leading to the nearly linear appearance of the black boundary line.

Sliding detachment occurs when the drag force exceeds the effective frictional resistance at the contact interface. This mode is more readily initiated than lifting detachment. The critical condition is predominantly influenced by two factors. Firstly, a reduction in the height-to-size ratio enhances wall confinement, leading to a significant increase in drag (partially offset by reduced lift) and consequently lowering the critical particle Reynolds number required for sliding. Secondly, the friction coefficient (μ) directly governs the sliding threshold: under the well-lubricated condition central to this study ($\mu = 0.11$), the critical particle Reynolds number $Re_{p,cri}$ is approximately 2. As lubrication diminishes and μ increases to 0.22, the critical boundary shifts toward a higher $Re_{p,cri}$, indicating that greater flow intensity is required to initiate sliding. The analysis of μ variation is presented here primarily for parametric illustration of its influence. Since rolling detachment is the most readily initiated mechanism under the investigated conditions, a detailed analysis of sliding across varying μ is not the primary focus of this work.

Rolling detachment is the most easily triggered mode, occurring at $Re_{p,cri}$ between 0.3 and 2, because the drag force has a large lever arm relative to the contact radius. This finding aligns with previous studies (Cui and Sommerfeld, 2015; Meng et al., 2022). A decrease in the height-to-size ratio also facilitates rolling, since the accompanying increase in torque and drag outweighs the slight decrease in lift. Higher surface energy strengthens adhesion and increases the contact radius, raising the $Re_{p,cri}$ for all detachment modes. Therefore, in engineering applications, promoting particle detachment, particularly through rolling, can be achieved by reducing surface energy, decreasing the height to size ratio, or increasing the particle Reynolds number.

To improve clarity amid the wide numerical range in Fig. 16, Fig. 17 is presented to highlight the influence of dimensionless adhesion forces and height-to-size ratios on the critical particle Reynolds number. This figure shows the critical Reynolds numbers required for lifting, sliding, and rolling detachment in confined Couette flow under varying adhesion and confinement conditions. For a fixed surface energy, reducing the height-to-size ratio from 6 to 1.5 raises the critical Reynolds number for lifting by up to 4.7 %, while decreasing those for sliding and rolling by up to 18.5 % and 16.6 %, respectively. This difference arises because wall effects have limited influence on lift attenuation at higher Reynolds numbers but strongly enhance drag and torque at lower Reynolds numbers. Moreover, increasing the surface energy from 1.5 J/m^2 to 2.7 J/m^2 strengthens adhesion, raising the effective normal force. As a result, at a height-to-size ratio of 6, the critical Reynolds numbers for lifting, sliding, and rolling increase by 46.2 %, 71.0 %, and 111.9 %, respectively. Similarly, at a ratio of 1.5, the corresponding increases are 47.2 %, 73.3 %, and 113.5 %.

Fig. 18 shows the relationship between adhesion force ratios and the corresponding critical particle Reynolds number ratios for lifting, sliding, and rolling detachment under two height-to-size ratios ($\kappa = 1.5$ in black, $\kappa = 6$ in red). Squares, circles, and triangles represent lifting, sliding, and rolling modes, respectively. Fig. 18(a) plots the ratio of each critical Reynolds number to its minimum value against the ratio of the adhesion force to its minimum value. A slope greater than 1 indicates that the critical Reynolds number increases more rapidly than the adhesion force. This explains the decrease in dimensionless adhesion force for rolling shown in Fig. 16: although absolute adhesion rises, the critical Reynolds number required for rolling increases at an even faster rate.

However, this absolute scaling may misleadingly imply sustained linear growth. To reveal the underlying trends, Fig. 18(b) plots the ratio of each critical particle Reynolds number to its preceding smaller value against the corresponding ratio of adhesion forces. All values exceed unity, confirming that critical Reynolds numbers increase monotonically with adhesion. More importantly, the growth rate decelerates for all detachment modes as adhesion increases, a subtle trend not easily discernible in Fig. 16. Rolling detachment exhibits the strongest deceleration, which stems from its very low baseline critical Reynolds number under minimal adhesion. At higher particle Reynolds numbers, increases in hydrodynamic forces and torques dominate over variations induced by wall effects. As a result, the influence of the height to size ratio becomes negligible. Finally, an algorithm to determine critical particle Reynolds numbers across specified height-to-size ratios and dimensionless adhesion forces is presented in Appendix A.

Table I
Properties of stainless steel and hydraulic oil.

Stainless steel	Surface energy (J/m^2)	1.5–2.7
	Young's modulus (GPa)	194
	Poison ratio (-)	0.3
	Atomic distance (nm)	0.28
	Density (kg/m^3)	8000
Hydraulic oil	Kinematic viscosity (m^2/s)	0.000046
	Density (kg/m^3)	850

6. Conclusions

This study investigates the effects of wall confinement on hydrodynamic forces and particle detachment in confined Couette flow using GPU-accelerated LBM for $\kappa = 1.5$–12 and $Re_p = 0.1$–40. The results show that wall confinement significantly alters the flow structure around the

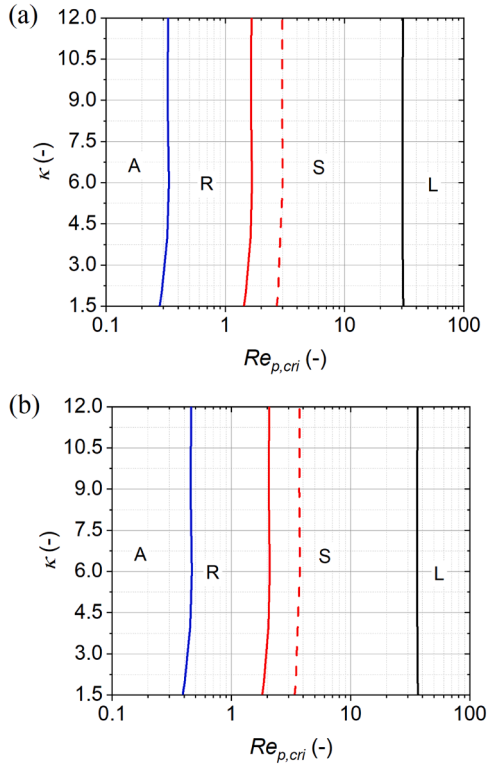


Fig. 16. In confined Couette flow, phase diagram of height-to-size ratio versus critical particle Reynolds number under varying adhesion forces: (a) $W_A = 2.1$ J/m^2; (b) $W_A = 2.7$ J/m^2. The blue solid, red solid, red dashed, and black solid curves represent the critical boundaries for rolling, sliding ($\mu = 0.11$), sliding ($\mu = 0.22$), and lifting detachment, respectively. Regions A, R, S, and L correspond to particle adhesion, rolling, sliding, and lifting states.

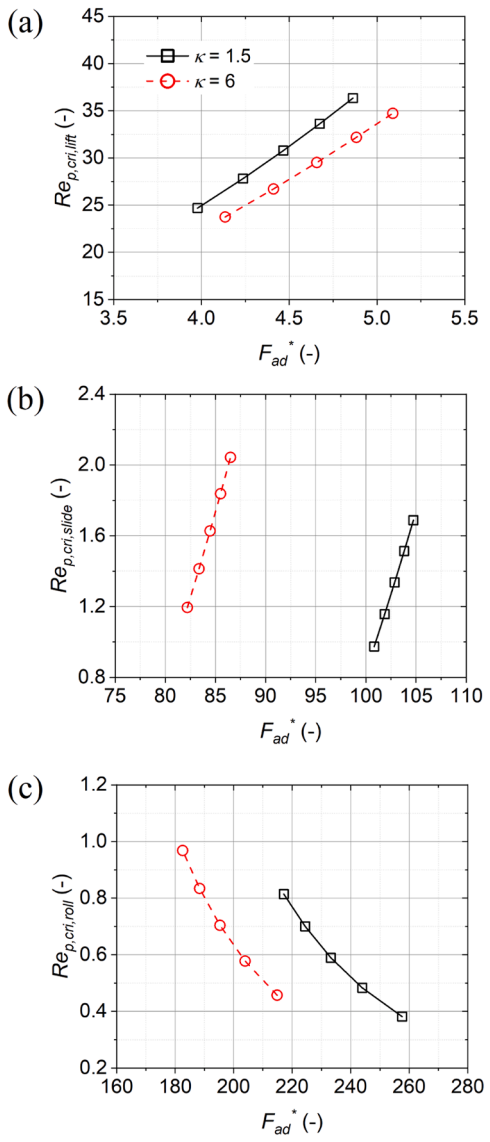


Fig. 17. The influence of the dimensionless adhesive force and the height-to-size ratio on the critical particle Reynolds numbers for lifting (a), sliding (b), and rolling (c) in confined Couette flow (W_A = 1.5–2.7 J/m^2).

particle, deflecting streamlines downward and shifting stagnation points upward, thereby reducing the flow velocity beneath the particle while accelerating it above.

Furthermore, wall confinement enhances the drag coefficient through an increased pressure differential between the windward and leeward surfaces, while markedly reducing the lift coefficient via suppression of vertical velocity. The torque coefficient experiences a minor increase due to enhanced asymmetry in the shear-stress distribution between the upper and lower particle surfaces. Notably, the substantial reduction in viscous lift leads to pressure-dominated lift characteristics even under weak inertial conditions. It is also observed that beyond κ = 6 the wall effects on drag and torque diminish, whereas the suppression of vertical velocity persists, rendering the lift coefficient more sensitive to wall spacing at low Re_p.

Rolling is identified as the most readily initiated detachment mode, and its critical condition decreases with stronger wall confinement. Additionally, empirical correlations for the force and torque coefficients and a predictive algorithm for critical detachment conditions in confined Couette flow have been developed. These tools can be integrated into Eulerian-Lagrangian computational frameworks to provide efficient and accurate predictions for contaminant control and removal in precision systems such as hydraulic components and microsensors.

Future research will extend the present framework to multi-particle interactions and more complex flow configurations (e.g., oscillatory flows), thereby enhancing its engineering applicability.

CRediT authorship contribution statement

Kun Meng: Writing – review & editing, Writing – original draft, Visualization, Validation, Software, Methodology, Investigation, Formal analysis, Data curation, Conceptualization. **Binbin Shan:** Writing – review & editing, Methodology, Investigation, Conceptualization. **Yan Cui:** Writing – review & editing, Supervision, Software, Resources, Methodology, Funding acquisition, Conceptualization. **Peng Gao:** Writing – review & editing, Visualization, Validation, Methodology, Investigation, Formal analysis, Conceptualization. **Chengjun Zhang:** Writing – review & editing, Software, Methodology, Investigation. **Xuyao Mao:** Writing – review & editing, Methodology, Investigation. **Jure Ravnik:** Writing – review & editing, Resources, Methodology, Funding acquisition, Formal analysis, Conceptualization. **Matjaž Hriberšek:** Writing – review & editing, Resources, Methodology, Investigation, Funding acquisition, Conceptualization. **Yinshui Liu:** Writing – review & editing, Resources, Funding acquisition, Conceptualization.

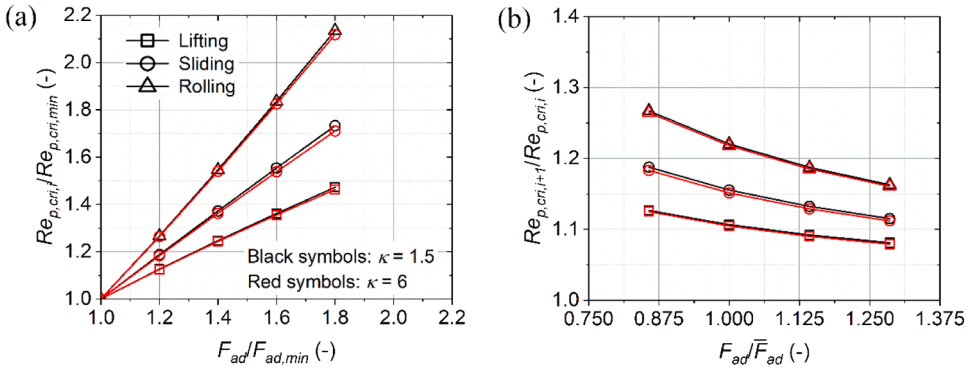


Fig. 18. The influence of the adhesion force ratio on the critical Reynolds number ratios for lifting, sliding, and rolling across different height-to-size ratios, where (a) illustrates the effect of the ratio of different adhesion forces to the minimum adhesion force on $Re_{p,cri,i}$ / $Re_{p,cri,\min}$, and (b) shows the effect of the ratio of different adhesion forces to the average adhesion force on $Re_{p,cri,i+1}$ / $Re_{p,cri,i}$.

Declaration of competing interest

The authors declare that they have no known competing financial interests or personal relationships that could have appeared to influence the work reported in this paper.

Acknowledgement

The authors acknowledge the financial supported by the General Program of the National Natural Science Foundation of China (Project No. 52576163) and ARIS Programme P2-0196.

Appendix A

From the user's perspective, it is important to determine the critical particle Reynolds number, which signifies the threshold at which particle initial detachment occurs. In this study, an algorithm is introduced, specifically designed to evaluate the critical particle Reynolds number in confined Couette flows. The corresponding procedure is illustrated by the flow chart in Fig. A1. This algorithm can be integrated into Eulerian-Lagrangian computational frameworks, improving both the computational efficiency and prediction accuracy for spherical particle detachment in precision fluid systems such as hydraulic components and microsensors.

1. Choose the input parameters, specifically the height-to-size ratio (κ) and the surface energy (W_A).
2. Compute the Tabor parameter using Eq. (20) and select the appropriate adhesion model, either the JKR model or the DMT model.
3. Determine the adhesion force (F_{ad}) and the contact radius (a) in accordance with the adhesion model selected in the previous step.
4. Initiate a loop by discretizing the range of particle Reynolds numbers into N values (i.e., $Re_{p,i}$, where i = 1:N). The value of N should be determined based on the required numerical precision for the critical particle Reynolds number.

4.1 Compute the drag coefficient using Eqs. (9) and (10), the lift coefficient using Eqs. (13) and (14), and the torque coefficient using Eqs. (16) and (17).

5.2 Compute the drag force, lift force, and hydrodynamic torque using Eq. (2).

6.3 Compute the lifting, sliding, and rolling ratios using Eq. (25), denoted as $\varphi_{lift}(Re_{p,i})$, $\varphi_{slide}(Re_{p,i})$, and $\varphi_{roll}(Re_{p,i})$.

5. Conclude the loop.
6. Identify the optimized particle Reynolds number at which the lifting, sliding, and rolling ratios are closest to unity; these specific particle Reynolds numbers represent the critical values for lifting, sliding, and rolling initial detachments (i.e., $Re_{p,cri,lift}$, $Re_{p,cri,slide}$, and $Re_{p,cri,roll}$).

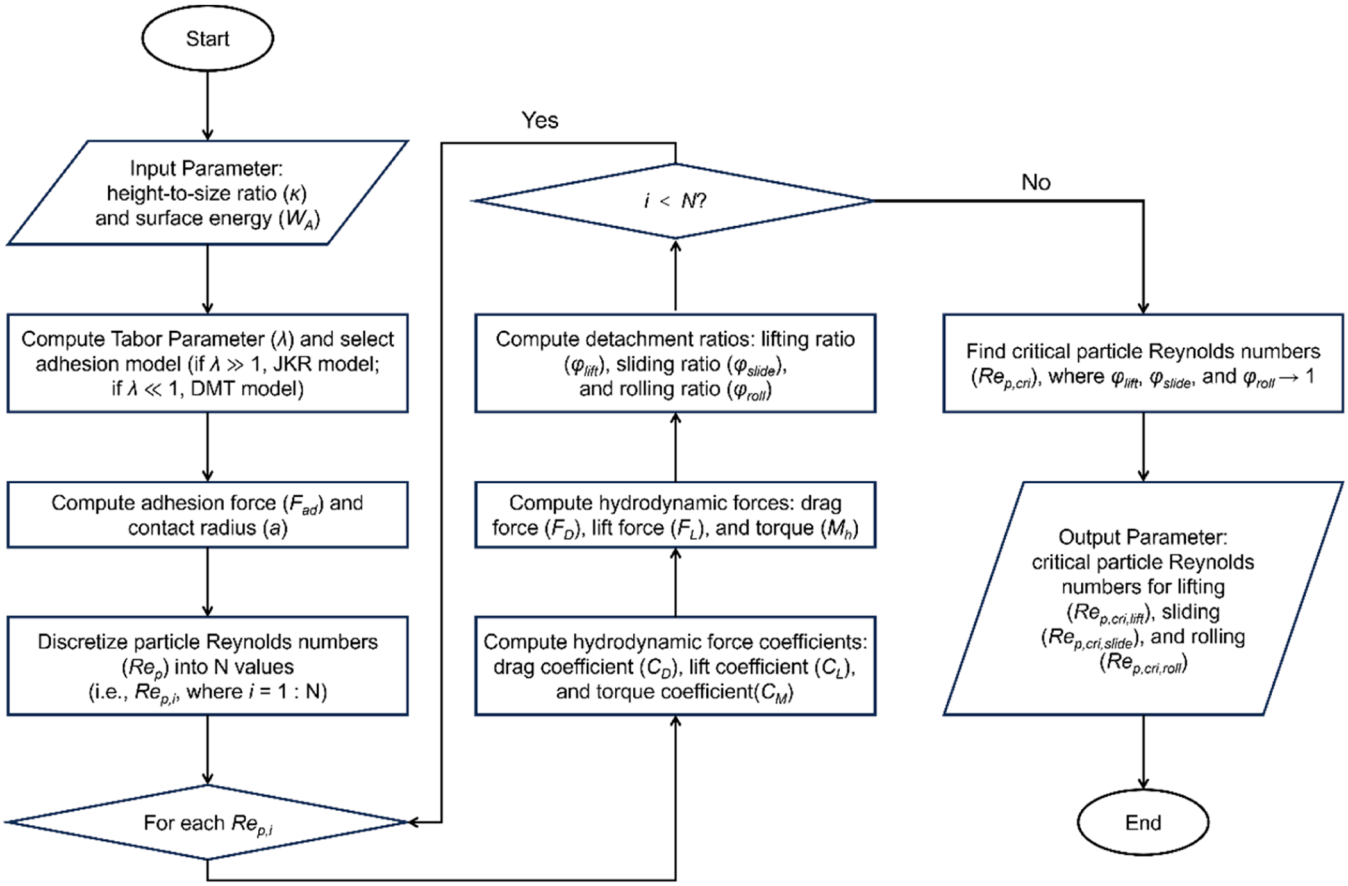


Fig. A1. Flow chart of the algorithm for determining critical particle Reynolds numbers.

Data availability

Data will be made available on request.

References

Anand, P., Subramanian, G., 2023. Inertial migration of a sphere in plane Couette flow. J. Fluid Mech. 977 (A33).

Asmolov, E.S., Dubov, A.L., Nizkaya, T.V., Harting, J., Vinogradova, O.I., 2018. Inertial focusing of finite-size particles in microchannels. J. Fluid Mech. 840, 613–630.

Bhagat, A.M., Goswami, P.S., 2022. Effect of rough wall on drag, lift, and torque on an ellipsoidal particle in a linear shear flow. Phys. Fluids. 34 (8).

Bhatnagar, P.L., Gross, E.P., Krook, M., 1954. A model for collision processes in gases. I. Small amplitude processes in charged and neutral one-component systems. Phys Rev 94 (3), 511.

Blaauw, L.J., Lohse, D., Huisman, S.G., 2025. Salts promote or inhibit bubbly drag reduction in turbulent Taylor–Couette flows. Int. J. Multiphase Flow. 184, 105078.

Chaoui, M., Feuillebois, F., 2003. Creeping flow around a sphere in a shear flow close to a wall. Q. J. Mech. Appl. Math. 56, 381–410.

Chen, G.F., Jiang, X.K., 2023. Single-particle dynamics in a low-Reynolds-number fluid under spherical confinement. J. Fluid Mech. 969 (A15).

Chen, Q.P., Liu, M., Ji, H., Chai, W.W., Luo, C.M., 2024. Characterization of hydraulic spool clamping triggered by solid particles based on mechanical model and experiment research. Appl. Sci. 14 (19), 8880.

Chen, S., Doolen, G.D., 1998. Lattice Boltzmann method for fluid flows. Annu. Rev. Fluid Mech. 30 (1), 329–364.

Chen, Y.X., Gong, W.J., Kang, R., 2016. Coupling behavior between adhesive and abrasive wear mechanism of aero-hydraulic spool valves. Chin. J. Aeronaut. 29 (4), 1119–1131.

Chequer, L., Carageorgos, T., Naby, M., Hussaini, M., Lee, W., Bedrikovetsky, P., 2021. Colloidal detachment from solid surfaces: phase diagrams to determine the detachment regime. Chem. Eng. Sci. 229, 116146.

Cherukat, P., McLaughlin, J.B., 1994. The inertial lift on a rigid sphere in a linear shear flow field near a flat wall. J. Fluid Mech. 263, 1–18.

Cox, R., Brenner, H., 1968. The lateral migration of solid particles in Poiseuille flow—I theory. Chem. Eng. Sci. 23 (2), 147–173.

Cui, Y., Sommerfeld, M., 2018. Application of lattice-Boltzmann method for analysing detachment of micron-sized particles from carrier particles in turbulent flows. Flow Turbul. Combust. 100, 271–297.

Cui, Y., Sommerfeld, M., 2015. Forces on micron-sized particles randomly distributed on the surface of larger particles and possibility of detachment. Int. J. Multiphase Flow. 72, 39–52.

Cui, Y., Sommerfeld, M., 2022. Lattice-Boltzmann simulations for analysing the detachment of micron-sized spherical particles from surfaces with large-scale roughness structures. Particuology 61, 47–59.

Derjaguin, B.V., Muller, V.M., Toporov, Y.P., 1975. Effect of contact deformations on the adhesion of particles. J. Colloid Interface Sci. 53 (2), 314–326.

Derksen, J.J., Larsen, R.A., 2011. Drag and lift forces on random assemblies of wall-attached spheres in low-Reynolds-number shear flow. J. Fluid Mech. 673, 548–573.

Ekanayake, N.I.K., Berry, J.D., Harvie, D.J.E., 2021. Lift and drag forces acting on a particle moving in the presence of slip and shear near a wall. J. Fluid Mech. 915, A103.

Ekanayake, N.I.K., Berry, J.D., Stickland, A.D., Dunstan, D.E., Muir, I.L., Dower, S.K., Harvie, D.J.E., 2020. Lift and drag forces acting on a particle moving with zero slip in a linear shear flow near a wall. J. Fluid Mech. 904 (A6).

Estepa-Cantero, C., Martínez-Bazán, C., Bolaños-Jiménez, R., 2025. Hydrodynamic forces on high Bond bubbles rising near a vertical wall at moderate Reynolds numbers: an experimental approach. Int. J. Multiphase Flow. 189, 105325.

Fillingham, P., Kottapalli, K., Zhan, X., Novosselov, I.V., 2019. Characterization of adhesion force in aerodynamic particle resuspension. J. Aerosol Sci. 128, 89–98.

Fillingham, P., Vaddi, R.S., Bruning, A., Israel, G., Novosselov, I.V., 2021. Drag, lift, and torque on a prolate spheroid resting on a smooth surface in a linear shear flow. Powder Technol 377, 958–965.

Fox, A.J., Schneider, J.W., Khair, A.S., 2021. Dynamics of a sphere in inertial shear flow between parallel walls. J. Fluid Mech. 915, A119.

Gao, P., Hu, R., Meng, K., Cui, Y., Mao, X., Liu, Y., 2025. Pitch angle effects on the detachment of a prolate spheroidal particle from a wall in linear shear flow. Phys. Fluids. 37 (6).

Gao, W., Shi, P.Y., Parsani, M., Costa, P., 2024. On the relevance of lift force modelling in turbulent wall flows with small inertial particles. J. Fluid Mech. 988, A47.

Goldman, A., Cox, R.G., Brenner, H., 1967. Slow viscous motion of a sphere parallel to a plane wall—II Couette flow. Chem. Eng. Sci. 22 (4), 653–660.

Goyal, A., Pierson, J.L., Wachs, A., 2024. Hydrodynamic force interaction of two fixed spheres in a wall-bounded linear shear flow. Int. J. Multiphase Flow. 172, 104720.

Guo, Z.L., Zheng, C.G., Shi, B.C., 2002. An extrapolation method for boundary conditions in lattice Boltzmann method. Phys. Fluids. 14 (6), 2007–2010.

Hafen, N., Thieringer, J.R., Meyer, J., Krause, M.J., Dittler, A., 2023. Numerical investigation of detachment and transport of particulate structures in wall-flow filters using lattice Boltzmann methods. J. Fluid Mech. 956, A30.

Happel, J., Brenner, H., 2012. Low Reynolds Number Hydrodynamics: With Special Applications to Particulate Media, 1. Springer.

He, X.Y., Luo, L.S., 1997. A priori derivation of the lattice Boltzmann equation. Phys. Rev. E. 55 (6), R6333–R6336.

Higuera, F.J., Jiménez, J., 1989. Boltzmann approach to lattice gas simulations. Europhys. Lett. 9 (7), 663.

Ho, B., Leal, L., 1976. Migration of rigid spheres in a two-dimensional unidirectional shear flow of a second-order fluid. J. Fluid Mech. 76 (4), 783–799.

Hubbe, M.A., 1984. Theory of detachment of colloidal particles from flat surfaces exposed to flow. Colloids Surf 12, 151–178.

d'Humières, D., 1994. Generalized lattice-Boltzmann equations. Rarefied Gas Dynamics: Theory and Simulations. AIAA, pp. 450–458.

d'Humières, D., Ginzburg, I., Krafczyk, M., Lallemand, P., Luo, L.S., 2002. Multiple-relaxation-time lattice Boltzmann models in three dimensions. Philos. Trans. A Math. Phys. Eng. Sci. 360 (1792), 437–451.

Johnson, K.L., Kendall, K., Roberts, A.A.D., 1971. Surface energy and the contact of elastic solids. Proc. R. Soc. Lond. A 324 (1558), 301–313.

Krishnan, G.P., Leighton Jr, D.T., 1995. Inertial lift on a moving sphere in contact with a plane wall in a shear flow. Phys. Fluids 7, 2538–2545.

Kosaku, Y., Tsunazawa, Y., Tokoro, C., 2023. A coarse-grain model with parameter scaling of adhesion forces from liquid-bridge forces and JKR theory in the discrete element method. Chem. Eng. Sci. 268, 118428.

Laín, S., Castang, C., Sommerfeld, M., 2024. Study of flow resistance coefficients acting on regular non-spherical particles in simple shear flow at moderate Reynolds numbers. Powder Technol 435, 119428.

Lauricella, G., Naderi, M.M., Zhou, J., Papautsky, I., Peng, Z.L., 2024. Bifurcation of equilibrium positions for ellipsoidal particles in inertial shear flows between two walls. J. Fluid Mech. 984, A47.

Lee, H., Balachandar, S., 2010. Drag and lift forces on a spherical particle moving on a wall in a shear flow at finite *Re*. J. Fluid Mech. 657, 89–125.

Legendre, D., Magnaudet, J., 1997. A note on the lift force on a spherical bubble or drop in a low-Reynolds-number shear flow. Phys. Fluids. 9 (11), 3572–3574.

Lehmann, M., 2022. Esoteric pull and esoteric push: two simple in-place streaming schemes for the lattice Boltzmann method on GPUs. Comput 10 (6), 92.

Lehmann, M., Krause, M.J., Amati, G., Sega, M., Harting, J., Gekle, S., 2022. Accuracy and performance of the lattice Boltzmann method with 64-bit, 32-bit, and customized 16-bit number formats. Phys. Rev. E. 106 (1), 015308.

Leighton, D., Acrivos, A., 1985. The lift on a small sphere touching a plane in the presence of a simple shear flow. Z. Angew. Math. Phys. 36 (1), 174–178.

Lin, Z., Li, R., Xia, Y., Ouyang, Z., Yu, Z., Lu, W., 2025. Numerical study of microorganisms swimming through viscoelastic fluids in a circular tube. Phys. Fluids. 37, 091903.

Liu, J.C., Zheng, M.Q., Ma, Y.L., Wang, J.W., Li, H.H., Zheng, H.D., Yan, Z.Y., 2025. Microreactor with coupled oscillatory flow: research on liquid-solid two-phase characteristics and clogging mechanism. Chem. Eng. Sci. 302, 120790.

Magnaudet, J., Takagi, S., Legendre, D., 2003. Drag, deformation and lateral migration of a buoyant drop moving near a wall. J. Fluid Mech. 476, 115–157.

Matas, J.P., Morris, J.F., Guazzelli, É., 2004. Inertial migration of rigid spherical particles in Poiseuille flow. J. Fluid Mech. 515, 171–195.

McLaughlin, J.B., 1991. Inertial migration of a small sphere in linear shear flows. J. Fluid Mech. 224, 261–274.

McLaughlin, J.B., 1993. The lift on a small sphere in wall-bounded linear shear flows. J. Fluid Mech. 246, 249–265.

McNamara, G.R., Zanetti, G., 1988. Use of the Boltzmann equation to simulate lattice gas automata. Phys. Rev. Lett. 61 (20), 2332–2335.

Meng, K., Pang, Y.Q., Liu, Y.S., Cui, Y., 2022. Hydrodynamic force and torque acting on a micron-sized spherical particle attached to a surface with large-scale concave roughness in linear shear flow and the possibility of detachment. J. Fluid Mech. 947, A27.

Novak, N., Trajkovski, A., Kalin, M., Majdič, F., 2023. Degradation of hydraulic system due to wear particles or medium test dust. Appl. Sci. 13, 7777.

O'neill, M.E., 1968. A sphere in contact with a plane wall in a slow linear shear flow. Chem. Eng. Sci. 23 (11), 1293–1298.

Ouchene, R., 2025. Contribution to the study of the dislodgment conditions of spheroids from a surface in fluid flow. Phys. Fluids. 37 (2).

Prokopovich, P., Perni, S., 2011. Comparison of JKR-and DMT-based multi-asperity adhesion model: theory and experiment. Colloids Surf. A. 383 (1–3), 95–101.

Qian, Y.H., d'Humières, D., Lallemand, P., 1992. Lattice BGK models for Navier-Stokes equation. Europhys. Lett. 17 (6), 479.

Rosa, F.S.S., Dalvit, D.A.R., Milonni, P.W., 2008. Casimir-Lifshitz theory and metamaterials. Phys. Rev. Lett. 100, 183602.

Saffman, P.G., 1965. The lift on a small sphere in a slow shear flow. J. Fluid Mech. 22 (2), 385–400.

Schiller, L., Naumann, A., 1933. Uber die grundlegenden berech-nungen bei der schwerkraftaufbereitung. Z. Vereines Deutscher Inge 77, 318–321.

Segre, G., Silberberg, A., 1962. Behaviour of macroscopic rigid spheres in Poiseuille flow Part 2. Experimental results and interpretation. J. Fluid Mech. 14 (1), 136–157.

Shi, P., Rzehak, R., 2020. Lift forces on solid spherical particles in wall-bounded flows. Chem. Eng. Sci. 211, 115264.

Shi, P., Rzehak, R., Lucas, D., Magnaudet, J., 2021. Drag and lift forces on a rigid sphere immersed in a wall-bounded linear shear flow. Phys. Rev. Fluids. 6 (10), 104309.

Stokes, G.G., 1851. On the effect of the internal friction of fluids on the motion of pendulums. Trans. Camb. Philos. Soc. 9, 8.

Sommerfeld, M., Taborda, M.A., 2024. Collision rates of small solid particles with rigid spherical and spheroidal bubbles in laminar flow. Exp. Comput. Multiphase Flow 6 (4), 365–386.

Su, J., Zheng, X., Hu, G., 2023. New explicit formula for inertial lift in confined flows. Phys. Fluids. 35 (9).

Tabor, D., 1977. Surface forces and surface interactions. J. Colloid Interface Sci. 58, 3–14.

Tang, G.H., Gu, X.J., Barber, R.W., Emerson, D.R., Zhang, Y.H., 2008. Lattice Boltzmann simulation of nonequilibrium effects in oscillatory gas flow. Phys. Rev. E. 78 (2), 026706.
Ting, H.Z., Yang, Y., Tian, Z.F., Carageorgos, T., Bedrikovetsky, P., 2023. Detachment of inclined spheroidal particles from flat substrates. Powder Technol 427, 118754.
van der Sman, R.G.M., 2010. Drag force on spheres confined on the center line of rectangular microchannels. J. Colloid Interface Sci. 351 (1), 43–49.
Vasseur, P., Cox, R.G., 1976. The lateral migration of a spherical particle in two-dimensional shear flows. J. Fluid Mech. 78 (2), 385–413.
Wang, P., Lei, Y.H.N., Zhu, Z.P., Zheng, X.J., 2023. Drag model of finite-sized particle in turbulent wall-bound flow over sediment bed. J. Fluid Mech. 964 (A9).
Wang, T., Lin, Z., Guo, Y., Yu, Z., 2025. Hydrodynamic forces on a spherical particle in a plane Couette flow. Int. J. Multiphase Flow. 192, 105341.
Xie, L., Zhang, Q., Zhang, J., Ji, C., 2018. Drag force and torque of a stationary sphere in a uniform laminar open channel flow. Phys. Fluids. 30 (12).
Ye, W.J., Wang, X., Hemmert, W., Freeman, D., White, J., 2003. Air damping in laterally oscillating microresonators: a numerical and experimental study. J. Microelectromech. Syst. 12 (5), 557–566.
Yin, Y.B., Yuan, J.Y., Guo, S.R., 2017. Numerical study of solid particle erosion in hydraulic spool valves. Wear 392, 174–189.
Yu, B., Xu, Z., Zhao, Z., 2025. Droplet evaporation on bio-inspired surfaces considering the electric field based on MRT-LBM. Int. J. Multiphase Flow. 189, 105267.
Yu, Z., Shao, X., 2010. Direct numerical simulation of particulate flows with a fictitious domain method. Int. J. Multiphase Flow. 36, 127–134.
Zeng, L.Y., Balachandar, S., Fischer, P., 2005. Wall-induced forces on a rigid sphere at finite Reynolds number. J. Fluid Mech. 536, 1–25.
Zeng, L.Y., Najjar, F., Balachandar, S., Fischer, P., 2009. Forces on a finite-sized particle located close to a wall in a linear shear flow. Phys. Fluids. 21 (3), 033302.
Zhang, J., Yuan, J., Yuan, H., 2025. Multi-physical field cross-scale simulation of brine freezing process in microchannel fluid flow considering suspended ice crystals. Int. J. Multiphase Flow. 189, 105254.